Exploring Halo Substructure with Giant Stars: II. Mapping the Extended Structure of the Carina Dwarf Spheroidal Galaxy

Steven R. Majewski[1,2,3,4], James C. Ostheimer[1], Richard J. Patterson[1], William E. Kunkel[5], Kathryn V. Johnston[6], and Doug Geisler[7]

ABSTRACT

As part of our survey for substructure in the Milky Way halo as traced by giant stars, and to look for tidal stellar debris in the halo viable for measurement of the Galactic mass potential with the Space Interferometry Mission (SIM), we explore the distribution of stars beyond the nominal tidal radius of, but still associated with, the Carina dwarf spheroidal galaxy. We make use of the photometric technique described in Majewski et al. (1999b, AJ, submitted) to identify giant star candidates at the distance and metallicity of the Carina dwarf spheroidal across the entire extent of a photometric survey covering some 2.2 deg^2 on and around Carina. These Carina-associated giant candidates are identified by a combination of (1) their $M - DDO51$ colors, which are a measure of both surface gravity and metallicity at given $M - T_2$ colors, and (2) by locations in the color-magnitude diagram commensurate with the Carina red giant branch in the core of the galaxy. The density distribution of the extratidal giant candidates bears resemblance to the outer isopleths of Carina presented by Irwin & Hatzidimitriou (1995, MNRAS, 277, 1354). However, in contrast to previous, *statistical* star-counting approaches, we can pinpoint *actual*, remotely-situated Carina stars individually. Because we can exclude the foreground veil of dwarf stars, our approach allows greater sensitivity and the ability to map the detailed two-dimensional distribution of extended Carina populations to much larger radii, while utilizing smaller aperture telescopes, than other techniques. Moreover, we identify candidate lists of widely displaced Carina-associated stars bright enough for spectroscopic studies of large-scale dynamical and metallicity

[1]Dept. of Astronomy, University of Virginia, Charlottesville, VA, 22903-0818 (srm4n@didjeridu.astro.virginia.edu, jco9w@virginia.edu, ricky@virginia.edu)

[2]Visiting Associate, The Observatories of the Carnegie Institution of Washington, 813 Santa Barbara Street, Pasadena, CA 91101

[3]David and Lucile Packard Foundation Fellow

[4]Cottrell Scholar of The Research Corporation

[5]Las Campanas Observatory, Carnegie Institution of Washington, Casilla 601, La Serena, Chile (skunk@roses.ctio.noao.edu)

[6]Dept. of Astronomy, Wesleyan University, Middletown, CT 06459-0123 (kvj@astro.wesleyan.edu)

[7]Department of Physics, Universidad de Concepción, Concepción, Chile (doug@stars.cfm.udec.cl)

properties of the system, and for astrometric study by SIM. We obtained spectroscopy for three such "extratidal" stars and from their radial velocities conclude that all three are associated with Carina.

While a single King profile matches our derived Carina core density profile, we confirm previous claims for a break in the density fall-off at about 20 arcmin. Beyond this radius, a more gradual fall-off as $r^{-\gamma}$, with $1 < \gamma < 2$, to $r \geq 80$ arcmin, is found. If the existence of density profile breaks is a signature of the predominance of unbound stars, and if we adopt the nominal tidal radius of 28 arcmin previously found for Carina, then it would appear that we have identified a substantial extratidal population from Carina. If these $r \gtrsim 20$ arcmin stars are truly now unbound from the galaxy, we estimate from the relative stellar density distribution a fractional destruction rate for Carina from tidal stripping of order $(\frac{df}{dt}) = 0.27$ Gyr^{-1}. This is among the highest rates expected for the Milky Way dwarf spheroidals apart from Sagittarius. The existence of such extended populations of Carina-associated stars may have important implications for the existence of large dark matter contents in dwarf spheroidals, as well as for the evolution of the Milky Way halo.

Finally, we find that the "background density" of what are likely to be predominantly random, metal-poor halo field giants maintains a rather flat count-magnitude relation out to the distance of Carina, in keeping with R^{-3} density laws for the Galactic halo.

Subject headings: Galaxy: evolution – Galaxy: formation – Galaxy: halo – Galaxy: structure – stars: galaxies: individual (Carina dSph) – photometry – stars: giants

1. Introduction

It is becoming increasingly clear that dwarf spheroidal galaxies are not the simple systems they were once thought to be. A great deal of recent work has exposed the complicated star formation histories in many of these small systems in the Local Group (see summaries by Grebel 1997, 1998, Mateo 1998). That a system like Carina, which has experienced at least three major episodes of star formation in its lifetime (Smecker-Hane et al. 1994, 1996, Mighell 1997, Hurley-Keller et al. 1998), can retain gas to fuel repeated bursts appears to contradict old notions of these low luminosity systems having fragile, fluffy mass potentials (see, e.g., Dekel & Silk 1986, Burkert & Ruiz-Lapuente 1997, MacLow & Ferrara 1999).

Indeed, dynamical studies of the mass-to-light, M/L, ratios of most of the Galactic dwarf spheroidals (e.g., Aaronson 1983, Seitzer & Frogel 1985, Aaronson & Olszewski 1987, Pryor & Kormendy 1990, Mateo et al. 1993, Suntzeff et al. 1993, Hargreaves et al. 1994, Vogt et al. 1995, Olszewski et al. 1996, Mateo et al. 1998b) imply large values, approaching $M/L \sim 100$ or more in the systems with the least total luminosity: Draco, Sextans and Ursa Minor (Olszewski, Aaronson & Hill 1995 and references therein, Irwin & Hatzidimitriou 1995, IH95 hereafter; Mateo 1998).

Clearly dwarf spheroidal galaxies are not just larger versions of globular clusters, which have typical $M/L \sim 1-2$, but are of a very different structural character. The structural difference between globular clusters and dwarf spheroidals has often been attributed to a large dark matter content in the latter.

However, the large dark matter interpretation of the large velocity dispersions observed in dwarf spheroidals is subject to various uncertainties and still debated. There are assumptions (see Vogt et al. 1995, Piatek & Pryor 1995, IH95, Kleyna et al. 1999) incorporated into typical M/L determinations that remain to be verified, including the assumption of isotropically distributed stellar orbits, that mass follows the distribution of light in these systems, and even that normal Newtonian gravity applies.[8] Moreover, unresolved binaries inflate derived velocity dispersions to some degree that may or may not affect M/L ratios significantly (Suntzeff et al. 1993, Olszewski, Pryor & Armandroff 1996, Hargreaves, Gilmore & Annan 1996).

Perhaps the greatest uncertainty in the dark matter interpretation of the velocity dispersion data is that of a virial equilibrium state for the dwarf spheroidals. The notion of dwarf galaxies in virial equilibrium has been questioned by, e.g., Kuhn & Miller (1989), who attributed the high velocity dispersions to orbital resonance "heating" of the stars in satellites, with a resulting inflation of the internal velocities. While this particular model has been controversial (Pryor 1999), the idea that passage of the satellites near massive objects like the Galactic center or dark matter clumps in the halo (Kroupa 1999) can affect the internal dynamics and outer structure of these dwarf galaxies has a long history.

For example, Hodge & Michie (1969) concluded that Galactic tides could have an important effect on the outer structure of dwarf spheroidals and suggested that Ursa Minor is presently in the throes of total disruption. Still, it is not clear to what extent tidal disruption can perturb the inferred dark matter content. For example, it is hard to understand how tides could be affecting such distant dwarfs as Leo I and Leo II, for which relatively large (~ 10), M/L are found (Vogt et al. 1995). In a numerical modeling study of the phenomenon of tidally induced, large velocity dispersions in dwarf spheroidals, Piatek & Pryor (1995) concluded that Galactic tides cannot account for extraordinarily large M/L, though an inflation of M/L to about 40 was possible. Johnston, Sigurdsson & Hernquist (1999b) similarly find little influence on the core velocity dispersions for tidally disrupting systems. The main influence of tides on the dynamics of the dwarfs is not to inflate central velocity dispersions, but rather to produce large ordered motions that would resemble apparent systemic rotations. Indeed, such shearing motions have been observed in the Ursa Minor and Draco systems by Hargreaves et al. (1994).

However, a contrasting point of view comes out of high resolution, N-body studies by Klessen & Kroupa (1998) of the dynamical evolution of satellite galaxies in Milky Way-like gravitational

---

[8]Milgrom (1983a,b) has proposed a form of Modified Newtonian Dynamics (MOND) that serves to reduce the implied M/L's of bound stellar systems.

potentials *followed until well after the disruption.* Klessen & Kroupa find that the debris of large satellite galaxies on orbits of eccentricities greater than 0.41 and undergoing severe tidal disruption eventually converge into stable remnants of about 1% the original satellite mass. When viewed along certain lines of sight, these remnants have properties very similar to dwarf spheroidal galaxies, including, most interestingly, velocity dispersions leading to *inferred* high M/L's *in spite of the fact that the remnants do not contain dark matter.* The notion that some of the Milky Way dwarf spheroidals may be tidal remnants has been discussed for several decades because of the seemingly non-random alignments of the satellites around the Milky Way (Kunkel 1979, Lynden-Bell 1982, Majewski 1994, Lynden-Bell & Lynden-Bell 1995, Palma, Majewski & Johnston 1999). While Klessen & Kroupa do not predict what the density profiles of their tidal remnants would look like, their scenario predicts that their dSphs should exhibit ordered radial velocity gradients across the galaxy, similar to those discussed above.

These issues have been confused by the discovery around the majority of the Milky Way dwarf spheroidals of "breaks" in the starcount profiles where the character of the counts changes from a steeply falling King profile to a much more gradual decline with radius (Eskridge 1988a,b; IH95). Such features are seen in simulations in which a satellite (with mass tracing the light) is being stripped by the Milky Way's tidal field (Oh, Lin & Aarseth 1995, Piatek & Pryor 1995, Johnston et al. 1999b), and it is tempting to attribute such breaks in the radial profile to the onset of an outer population of escaping stars.[9] On the other hand, arguments have been made that the existence of tidal tails is evidence against the presence of significant dark matter halos in dwarf spheroidals (Moore 1996, Burkert 1997). If the satellite contained sufficient dark matter, then the point at which tidal effects became important would lie well beyond the "tidal radius" found from King model fits to the luminous matter. As Moore (1996) concludes: "...even modest amounts of dark matter will be very effective at containing the visible stars and halting the production of tidal tails."

Whatever the solution to these contradictory and confusing issues, it is certain that more observational handles on the problem would help with clearing the theoretical hurdles. For example, if the outer populations of the dwarf spheroidals could be mapped well past the break radius, it may become evident whether they evolve into obvious tidal tails. Measuring the velocities of stars beyond the break would also provide a great advantage to discriminating between models. For example, evidence for shearing motions, as described above, would support tidal tail models, while isotropic velocity dispersions would support the notion that the beyond-the-break populations are bound. Both mapping dwarf galaxies to large radii and obtaining velocities of well separated, but associated stars are among the goals of the present program, which has an overall aim to employ various strategies to uncover tidal debris from disrupting satellite galaxies.

---

[9]It is worth noting one interesting exception to this attribution. In an earlier study of the extratidal phenomenon with van Agt's (1978) sample of extratidal stars around Sculptor, Innanen & Papp (1979) concluded that stars outside the tidal radius could still be bound if on retrograde orbits about the satellite. Stars on such orbits can resist tidal stripping by the Milky Way.

In this contribution we present the first results of a search for widely extended, beyond-break-radius stars associated with nearby dwarf galaxies, with a focus on a survey around the Carina dwarf spheroidal. Carina was discovered from UK Schmidt plates by Cannon, Hawarden, & Tritton (1977). Demers, Beland, & Kunkel (1983) determined the following structural parameters (from star counts off of prints of a CTIO 4-m plate) out to a radius of ~ 38 arcmin along the semimajor axis: an ellipticity of 0.4 at a position angle of 75°, and a tidal radius of 33 arcmin. IH95 examined Carina's structure via star counts out to a radius of ~ 40 arcmin using APM scans of Schmidt plates and found similar structural parameters: an ellipticity of 0.33 at a position angle of 65°, and a tidal radius of 28 arcmin. Most significantly, IH95 found a clear break in the radial starcount profile and suggested the existence of an apparent extratidal population. Kuhn, Smith & Hawley (1996) noted a spatially extended RR Lyrae distribution for Carina (though all of their RR Lyrae were interior to the IH95 tidal radius), and with a more sophisticated starcount analysis gave even more compelling evidence for an extratidal Carina population extending some four tidal radii along the major axis, twice as far out as measured by IH95. From theoretical considerations of the observed structural parameters of Galactic dwarfs in IH95, Johnston et al. (1999b) designated Carina as one of the likely Galactic dwarf spheroidals with among the highest current fractional destruction rates. Given these various encouraging indicators, Carina is a promising first candidate to test our search technique for true tidal debris among the Galactic dwarf spheroidals.

We have reported elsewhere (Majewski 1999, Majewski et al. 1999c) preliminary results from our search for tidal debris around the Magellanic Clouds. Our overall strategy for finding extratidal stars differs from previous efforts in that we specifically target *giant stars* associated with the dwarf galaxies. This allows us to cover large areas of the sky efficiently with small telescopes, as we do not require deep imaging: Only the top several magnitudes of the red giant branch (RGB) of each galaxy are sought. The giant stars are identified photometrically using the three filter, Washington $M, T_2 + DDO51$ system described in Majewski et al. (1999b; "Paper I" hereafter). While perhaps more prone to small number statistics because of more restricted sample sizes, our technique confers certain advantages over the deep imaging, "CMD-differencing" strategies employed by, for example, IH95, Kuhn et al. (1996), Grillmair et al. (1995; see also Grillmair 1998), and others, that depend on uncovering *statistical* excesses of starcounts (either total starcounts or counts in particular regions of color-magnitude space). The latter type studies are especially sensitive to the zero-point level of, and variations in, the stellar starcount background (see, e.g., the discussions on this point in IH95). On the other hand, our goal is to pinpoint *actual* extratidal candidates individually (not statistically) by their signal as giant stars with properties expected for giants associated with the dwarf galaxy. By weeding out the overwhelming foreground curtain of dwarf stars, our approach is not only less susceptible to background subtraction problems and thereby capable of probing to larger radii more easily, but we also generate candidate lists of *bona fide* extratidal giants that are bright enough for spectroscopic verification and study. Thus, our approach fulfills the above stated strategies of mapping to large radii as well as providing good candidates for spectroscopy to do dynamical tests.

A campaign of targeted searches for extratidal stars and tidal tails around Galactic dwarf galaxies is of interest for numerous reasons. First, it is important to understand the extended structure of the dwarf spheroidals as leverage on the dark matter issues outlined above. Indeed, because we identify specific "extratidal" targets suitable for radial velocity measurement, we hope to be able to test directly whether they are bound to the dwarfs or not on the basis of the differences in the expected dynamical signatures. If unbound, we may then proceed to test the various models (e.g., Oh et al. 1995, Piatek & Pryor 1995, Hamlin 1997, Johnston 1998, Johnston et al. 1999b) of dwarf spheroidal disruption that make specific predictions of the velocity characteristics of these stars.

Second, the discovery of substantial tidal tails associated with Galactic satellites would provide the opportunity to measure the shape and size of the Galactic mass potential with unprecedented accuracy (Johnston et al. 1999c). An advantage conferred by our survey approach is that we can identify actual tidally-stripped stars that are viable candidates (i.e., bright enough) for proper motion measurement via the Space Interferometry Mission; a sample of some 100 such stars along a tidal tail with fully measured space velocities (to 10 km s^{-1} accuracy) can yield a measure of the mass of the Milky Way to a few percent accuracy in the region that the satellite's orbit explores. Hence, with several such tidal tails we could map the shape and size of the Milky Way with unprecedented accuracy.

Finally, the possibility of ongoing destruction of globular clusters and satellite galaxies has great bearing on the understanding of the formation and evolution of our own Milky Way. It is of interest to know what contribution is made to the Galactic halo from the destruction of satellites and accretion of their remains. The substantial ongoing contribution to the Milky Way of stellar and cluster debris from the Sagittarius dwarf galaxy, with a tidal tail now mapped to some 40° from the galaxy core (Mateo, Olszewski & Morrison 1998a; see also Majewski et al. 1999d, Johnston et al. 1999a) is likely not peculiar to the present epoch.

2. Photometry

The observations obtained for this project were accumulated over several observing runs at the Las Campanas Observatory, when small blocks of observing time were available (due to airmass, twilight, and weather considerations) during other programs. We include data from both the Swope 1-m (C40) and du Pont 2.5-m (C100) telescopes. Observations on the C40 were made with the same SITE#1 CCD and filters as employed in Paper I. On the C40, this CCD gives 23.8 arcmin per side field-of-view. Data were taken during grey or bright time on the nights of UT 10 March 1999 and 28 April to 3 May 1999. Data on the former run were photometric, while the CCD fields observed during the latter run were not photometric. In most cases, CCD fields overlapped with neighbors so that color/magnitude consistency could be checked. For each C40 field, exposures of 120, 120, and 1200 seconds were taken in each of the Washington M, T_2 and $DDO51$ filters. All frames were reduced with the stand alone version of DAOPHOT II (Stetson 1992) which produces

point spread function-fitting (PSF) photometry. Figure 1 shows the distribution of all detected stars in celestial coordinates; the lines show the boundaries of the various CCD frames (*solid* lines show frames taken during photometric conditions and *dashed* lines show frames take during non-photometric conditions). The density of detected stars at different points in Figure 1 are a function of the relative contribution of Carina, the relative proximity to the Galactic plane (Carina is at a Galactic latitude of $b = -22°$), the inclusion of both C40 and (deeper) C100 data, and the degree of cloudiness and seeing, which affects the limiting magnitudes of the C40 data.

The PSF-fit magnitude measures were calibrated against Geisler (1990) standards. For the data taken during photometric conditions, photometric transformation equations including airmass, color terms and nightly zero-point terms were determined. We followed the calibration procedures described in Majewski et al. (1994), using a similar matrix inversion algorithm (Harris, Fitzgerald & Reed 1981). The resultant transformation equations were applied to all of the photometric frames. A comparison of instrumental magnitudes in the CCD frames taken during cloudy weather to the fully transformed magnitudes on the photometric frames allowed derivation of frame-by-frame color and magnitude offset terms for the former data; thus the CCD data taken during non-photometric conditions were locked into the system of the calibrated photometric magnitudes. Figure 1 shows the geometry of photometric and bootstrapped fields. Note that the photometric frames were located in the center field and in a ring of fields separated from the center. Non-photometric frames overlapping multiple photometric frames were matched to all simultaneously. When final calibrations of all frames were achieved, a comparison of the derived magnitudes for stars in all overlapping regions between CCD frames showed no major discrepancies: the mean frame-to-frame offsets were typically of order 0.01 magnitudes. Nevertheless, for our final catalogues we adopted the magnitude measures for multiply photometered stars from the photometric frames over the non-photometric frames, whenever possible.

The du Pont 2.5-m observations were made on the night of UT 11 March 1999 with the new Wide Field Camera (WFC) system built by Ray Weymann and collaborators. The WFC delivers a useful circular field-of-view some 23 arcmin in diameter. Four fields were observed: one centered on the Carina core, two 50 arcmin along the major axis and outside the tidal radius (adopting the structural parameters found by IH95), and one along the minor axis at the same distance. The locations of these frames are shown by the circular fields in Figure 1. During the early operation of the WFC a residual misalignment of the field flattening lens with respect to the instrument axis shifted the center of symmetry of optimal focus slightly away from the center of the CCD frame, leaving the edge of one quadrant with somewhat deteriorated image profiles of sufficient severity that PSF-fitting photometry produced unsatisfactory results, even after allowing for PSF variation with a quadratic dependence on position in the CCD frame. We decided to optimize our DAOPHOT solutions to give good results over a large fraction of the CCD field and sacrifice the ability to work with the bad portion of the image, rather than trying to salvage the bad part of the field at the expense of less than satisfactory PSF-fitting over the entire field. Thus, as may be seen in Figure 1, the C100 data show a decline in the number of detections to the upper left of

each circular field. While this compromise means we lose stars from our survey, there should be no preference for losing giants compared to dwarfs.

While the C100 data were taken during photometric conditions, limited access meant there was no opportunity to obtain corresponding calibration frames. Fortunately, however, several of the C100 frames overlap with the photometrically calibrated C40 grid, and from these overlaps transformation equations could be derived for the C100 data. The latter were applied to all C100 frames, whether they overlapped the C40 data or not. Note that in the case where a star was photometered on more than one set of CCD frames, a weighted average of the magnitudes from the different frames was taken.

The photometric errors in the C40 and C100 data as a function of magnitude for each filter are shown in Figure 2a for the C40 data and Figure 2b for the C100 data. It can be seen that the C40 data, in particular, show a wide range in quality.

We remove from further consideration all detected objects with non-stellar image profiles. This was determined by deriving the running mean (in a 50 star "boxcar" filter) of the DAOPHOT II χ and sharp parameters as a function of magnitude and rejecting 3σ outliers from this mean for the C40 data. However, because of the problems with the image quality on the C100 frames, we took a more conservative rejection limit of 2.3σ. In addition, at this point we exclude all stars that have magnitude errors in any filter that are larger than 0.1 magnitudes. The latter cut is effectively one in magnitude (Figure 2) for each CCD field.

The $(M - T_2, M)_0$ color-magnitude diagram (CMD) for the C40 data for the area shown in Figure 1 is shown in Figure 3a; the total CMD for the C100 data, which probe some 2 magnitudes deeper, is shown in Figure 3b. Each star has been corrected for reddening based on its celestial coordinates and a comparison to the Schlegel et al. (1998) reddening maps. The precision of the photometry is typically about 0.04 magnitudes at $M = 19$ for the C40 data (but with a wide spread about this depending on the particular frame – see discussion of the relative magnitude limits below), and 0.03 magnitudes at $M = 19$ for the C100 data. The C100 data go deeper than the Carina horizontal branch (HB) at $M \sim 20.5$, while the Carina red clump is just barely detected in the C40 data. Figures 3c and 3d show the CMDs for the stars actually used in our survey , after application of the selection criteria described above.

3. Identification of Carina Giant Star Candidates

Our strategy for identifying likely extratidal giant stars associated with Carina tidal debris involves the application of two basic criteria: (1) stars must have magnesium line/band strengths consistent with those for giant stars with the abundance of Carina, and (2) stars must have combinations of surface temperatures and apparent magnitude consistent with the red giant branch of Carina. We apply these criteria in succession:

3.1. Giant Star Discrimination in the Two-Color Diagram

Paper I describes the method by which dwarf/giant separation can be achieved through the three filter imaging technique employed here. The basis of our technique lies in the sensitivity of the $DDO51$ filter to the MgH band (bandhead at 5211 Å) and Mg b triplet near 5150 Å (McClure 1976). These magnesium features are sensitive to stellar surface gravity (primarily) and temperature and abundance (secondarily) in later type stars. When combined with the wideband M and T_2 filters of the Washington system, the $DDO51$ filter is especially useful for discriminating giant stars from foreground dwarfs on the basis of differences in their respective $M - DDO51$ colors at a given $M - T_2$ color. The former color measures the strength of the magnesium line/band strength (where M acts as a suitable "continuum" measure for comparison to $DDO51$; Geisler 1984), while $M - T_2$ is sensitive primarily to stellar surface temperature (and is almost a linear scaling of $V - I$; Paper I). With this photometric system, it is possible with great efficiency to isolate giant stars at the distance of Carina with small telescopes, even in bright, moonlit skies as we had for the Carina observations here.

In Figure 4 we show the dereddened two-color diagram for both our C40 and C100 data, after pruning the sample with the error and image shape criteria described above. Figure 4 shows the characteristic "elbow-shaped" locus of dwarf stars (Paper I), which typically have the largest magnesium absorption at any given temperature. The region enclosed by the box drawn with thick solid lines is the general area in the two-color diagram inhabited by evolved, cool stars more metal-poor than [Fe/H]~ -0.5 (Paper I). The curved loci of giant stars of different abundances, as determined from the synthetic photometry of Paltoglou & Bell (1994) and presented in Paper I are overlaid for comparison. We note that Carina is established to have [Fe/H]$= -1.99$ with a dispersion of 0.25 dex, based on spectroscopic observations of 52 giants by Smecker-Hane et al. (1999). The diagonal, blue boundary of the "giant region" we have selected here is a somewhat conservative compromise to produce relatively uncontaminated giant candidate samples, while not sacrificing too many lower luminosity, bluer giants: The line is approximately parallel to the center of the near-solar metallicity dwarf locus, but offset by about +0.1 mag in $(M - DDO51)$ to account for typical magnitude errors at the faint end of the data sets. We now consider only stars in this delimited giant region as our first selection for metal-poor giants in our survey fields. As will become evident below, this giant star "bounding box" selects not only Carina stars on the RGB, but also Carina red clump stars.

While the goal of our three filter photometry is to cast exclusively for giant stars associated with Carina, our selection criterion in Figure 4 will also bring some contaminants into our net. Obviously, we will catch *any* giants with metallicities approximately like that of Carina. There will also be some dwarf contamination due to several-σ photometric errors scattering dwarfs into our giant star selection box. Finally, as may be seen from the lines in Figure 4, metal-poor subdwarfs with [Fe/H] $\lesssim -2.5$ also get pulled into our net. We expect the number of the latter type stars to be quite small, based on the very small fraction of halo stars with metallicities this poor. From Reid & Majewski (1993), the number of halo stars expected down to $V = 20$ over 2.2 deg^2 is about

590. However, only a small fraction ($\lesssim$ 10%) of these halo stars will be cool enough (spectral type K and later) to have an $(M - T_2)_0$ color which would place them in the giant bounding box, and only about 8% of *these* would be expected to have metallicities as low as [Fe/H] $\lesssim$ 2.5, according to Beers (1999) and Norris (1999). This leaves an expected level of contamination of $\lesssim$ 5 metal-poor subdwarfs in our entire survey area. We conclude that the vast majority of brighter non-Carina stars we select with only a color-color criterion will be random field giants, while at faint magnitudes we will pick up some dwarfs with extreme photometric errors. Eventually, either of these two types of contaminants will be readily identifiable through spectroscopy by their radial velocities (field giants) or line strengths (photometric error dwarfs). In another part of our halo observational program, we have done a search for tidal stellar debris from the Magellanic Clouds (Majewski et al. 1999a; see Majewski et al. 1999c). This part of our program includes both a photometric search for giants, as we have done here, as well as follow-up spectroscopy of the giant candidates. It is worth pointing out that in our Magellanic Cloud survey, which has identical photometric material to that which we have used here, we have found a very high success rate in the fraction of our giant candidates that we find to have spectroscopic line strengths and velocities like metal poor, halo giants. We expect similar, or better, success rates here since in the Magellanic Cloud work we used only aperture photometry, not PSF-fitting photometry as we used here, and in that other work we also allowed a more liberal selection (a larger "giant box") in the two-color diagram.

As a final check on the quality of the dwarf/giant discrimination with our photometric technique, we consider the sample of 23 candidate Carina RGB stars observed spectroscopically by Mateo et al. (1993). They chose these stars to lie near the top of the Carina RGB in the $(B-V, V)$ CMD, and found that 17 of the candidates had radial velocities consistent with Carina membership, while six had heliocentric velocities clustered around 0 km s^{-1}, consistent with their being foreground dwarfs (see their Figures 3 and 4). All of these stars were photometered by us, and we find that all 17 of the Carina RGB members (from Mateo et al.) are clearly giants in our two-color diagram (Figure 5, filled circles), while all 6 of the "foreground" stars of Mateo et al. are clearly dwarfs (open circles). We note that even while our photometry for several of the stars observed by Mateo et al. had errors that were too large to keep them in our formal sample, the colors of these stars still lie in the proper part of the color-color diagram, as seen in Figure 5. This comparison gives confidence that with our technique we can easily separate metal-poor giants from the typical foreground dwarf to produce very "clean" lists of RGB candidate stars suitable for followup spectroscopy.

3.2. The Color-Magnitude Locus of the Carina Red Giant Branch

We now use our own photometry of Carina *itself* to establish the expected location of associated evolved stars in the color-magnitude diagram. Figure 6 shows the color-magnitude distribution of all stars selected as giants in Figure 4, but within 10 arcmin (roughly the core radius) of the center of Carina for both the C40 and C100 data. Note that we measured the center of Carina from our

own data by fitting marginal distributions, but, as our determined center agreed to within 1 arcmin of the IH95 determination, for consistent comparisons we adopted the IH95 Carina center for all calculations from here on. We apply the 10 arcmin radial cut here to ensure that we obtain as pure a sample of bound Carina stars as possible for defining the Carina RGB region in the CMD. As can be seen by Figure 6, the selection of "giant star candidates" by the color-color technique seems to do a reasonable job of isolating a relatively "clean" sample of evolved stars: Very few stars fall outside the general region dominated by the Carina RGB in the CMD. Those stars falling away from the Carina RGB may either be dwarf stars that failed our giant discrimination due to photometric error or intrinsic properties ([Fe/H] $\lesssim -2.5$ dwarfs that show $M - DDO51$ colors of moderately metal-poor giants), they may be field giant stars, or they may be Carina giants with several-σ errors in their photometry.

Based on the location of the primary locus of Carina RGB stars in Figure 6, we may now apply a second, *color-magnitude* selection criteria to our giant star candidate sample, since, presumably, any RGB stars associated with Carina, no matter how far from the core of Carina and within our data set, should resemble RGB stars in the CMD of the Carina core. We note that the expected timescale ($\lesssim$ 1 Gyr) for tidal drift from Carina within the angles we survey are shorter than the enrichment timescale (Gyrs). Moreover, at present there is no evidence for an age-metallicity relation among the variously aged populations in Carina (Smecker-Hane et al. 1994, Da Costa 1994). We also expect stars in tidal tails to be lying within a few physical tidal radii (a few kpc) of the Carina core along the line of sight; these differences in distance would be virtually indistinguishable with our photometry. Only in very particular circumstances – e.g., looking along Carina's orbit – would we expect to see tidal debris to be highly elongated along the line of sight (for an example of the typical geometry of streamers around a satellite see Johnston 1998, Figure 3).

From the Carina core RGB distributions in Figure 6 we define a *CMD bounding box*, shown by the solid lines. This region (assembled from the combination of three second order polynomials) was defined to contain the bulk of the Carina core RGB locus, as well as the apparent red clump on the bluest end.

This same box may now be applied to the *entire* giant star candidate sample over 2.2 deg^2 from §3.1 to pick from among them those that, in addition to being pre-selected as evolved stars by their colors, *are of the correct magnitude for their color* to be associated with Carina (i.e., of an appropriate abundance/distance combination). Note that the actual size and shape of the bounding box utilized here does not really matter as long as it is applied consistently at all places in our survey mapping (Figure 1); in §3.4 we account for the level of contamination by background/foreground stars, which scales with the size of the box. A box that is too large simply allows more contamination into our final selection of Carina-associated stars. While this translates into a lower efficiency for follow-up spectroscopy of the selected sample, the increased contamination level may be removed in a statistical way by appropriate background subtraction. On the other hand, a box that is too restrictive means that more Carina-associated stars may be lost, and may decrease the signal-to-noise of our extended stellar population discussed below. Again, we have attempted to compromise

between these extremes, except that we erred on the side of making the box a "loose fit" to the RGB locus to account for the fact that extratidal stars may acquire *slightly* different mean distances as they get drawn out with different energies, ahead of or behind the parent object (e.g., as suggested by the bridge/tail description of Toomre & Toomre 1972).

3.3. "Carina-Like" Giant Candidates in the Two-Color and Color-Magnitude Diagrams

Figure 7 shows the primary locations of the core Carina RGB, as selected by the CMD-selection box in Figure 6. We see that the color-color distribution of these stars is smaller than the entire "giant box" in the two-color diagram, and one could conceive of narrowing the color-color selection criterion further by collapsing the giant box around the Carina locus. We do not do so here, however.

We now apply the selection criteria defined by the bounding boxes in both Figures 4 and 6 to the entire sample of stars in the C40 and C100 data sets to define the sample of most likely Carina-associated stars. In Figure 8 we show the CMDs of all C40 and C100 stars satisfying the two-color selection criterion in Figure 4 – i.e., all stars selected as evolved stars of similar metallicity to Carina in our entire survey area. Even when all evolved stars from the entire survey are included in the CMD, the dominant CMD structure, particularly for cool stars, is the Carina RGB. We include in Figure 8 the CMD selection criterion given by the bounding box selected in Figure 6. We note that it encloses most of the apparent Carina RGB, as expected. However, a notable exception is the trio of stars at $M_o \sim 17.5$ and $(M - T_2)_o > 1.85$: Though these three stars appear to be an extension of the Carina RGB bounding box, the latter does not extend red enough to include them because there were no examples of such relatively rare stars in the Carina core. Though we have formally excluded these stars in our analysis, we do consider these three stars as likely Carina-associated stars that we would have found with an appropriately-extended CMD bounding box. We return to discuss these stars in our spectroscopic tests in §3.5.

3.4. Sky Distributions and Evaluation of Giant Background Level

Figure 9a shows the distribution on the sky of all stars selected by our combined color-color-magnitude selection. The central fall off in the concentration of Carina giant candidates is obvious, but the fall off does not truncate completely, and, indeed, the density of candidates seems to flatten out and extend not only beyond the core radius, but the tidal radius as well. By comparison, we show in Figure 9b the stars that have similar color-color characteristics as Carina giants (i.e., within the box in Figure 4) but *outside* the CMD bounding box in Figure 6, i.e., stars that would be metal-poor giants, but generally at different distances than Carina. The latter show no central concentration, but rather, for the most part, the (expected) random, flat distribution of halo field

giants.

At first, the similarity of the distribution of the relative stellar density in the outer parts of Figure 9a and Figure 9b may appear to be a cause for concern. Some of the similarity is related to the differing depths of the individual CCD fields, which modulate both the number of detected Carina-associates and non-associates. Moreover, there could be some "spill-over" of true Carina stars to just outside of our selection criteria, which moves them from panel 9a to panel 9b. But of most concern to our purpose here is what fraction of the extratidal stars in Figure 9a are likely to be real and how many are expected to be "interlopers" – e.g., (1) dwarf stars that are accidentally selected to be "Carina-like" giants due either to photometric errors or extremely low [Fe/H], or (2) actual giant stars that happen to have the correct color/abundance/distance characteristics that place them into our sample? We must evaluate the expected level of contamination from interlopers, and we do so by monitoring the "background level" of such stars as a function of magnitude.

Before continuing, however, we must stress that the sky distributions of candidate giant stars as illustrated in Figure 9 are modulated by the variable depth of our data across the entire survey area and Figure 9a, even if accurately depicting the existence of extratidal Carina debris, cannot be interpreted as a mapping of the true relative density of that debris. Our analysis must proceed by taking into account the relative depths of our somewhat inhomogeneous data set. We do so by analyzing the survey with four different magnitude limits. At each magnitude limit, we include only those survey areas that are complete to that depth. The net effect of this approach is that with an increasing magnitude limit we cover less area on the sky, but we are able to recover greater densities of potential Carina-associated stars in the smaller areas because we probe further down the RGB. The goal of analyzing different magnitude-limited data sets in this way is a fair appraisal of not only the expected contamination levels, but the true relative sky densities of giant stars, while taking maximal advantage of the area covered at various depths.

Figure 10 shows the sky distributions of color-color-magnitude selected Carina-associated giant candidates taking into account the magnitude limits of the frames. For comparison, Figure 11 shows the same for all stars selected as metal-poor giants in the color-color diagram, but which are not along the Carina RGB in the color-magnitude diagram (i.e., presumably metal-poor giants at different distances than Carina). In Figure 10a and perhaps Figure 10b, it can be seen that the brighter, candidate Carina-associated stars do seem to show an overall radial drop-off from the core, but one that continues beyond the nominal tidal radius of IH95 (compare to the presumably "random field" star distributions in Figures 11a and 11b). For simplicity during the remainder of the discussion in this Section, we will refer to these stars outside the IH95 tidal radius as "extratidal", though we acknowledge the controversy regarding the true tidal radii of dwarf galaxies like Carina, as discussed in §1. Unfortunately, it is more difficult to follow any apparent radial trend in the deeper survey fields shown in Figures 10c and 10d, because of the poor radial sampling in the placement of the fields. On the other hand, it can be seen that the total number of extratidal giant candidates in Figures 10c and 10d outnumber the stars in the same regions of the sky in Figures 11c and 11d, respectively. This is significant because the relative areas in the color-magnitude diagram

from which the extratidal giants are culled is much smaller in Figure 10 than in Figure 11. Thus, it would appear, we are seeing a significant excess in extratidally-positioned stars at just the colors and magnitudes expected for Carina-associated populations.

To put the latter assessment on a more quantitative footing, we assess in Figures 12 and 13 the background contribution of field giant stars (and the expected small contribution of foreground dwarfs from photometric error and extreme subdwarfs) to our counts of candidate Carina-associated giants. The foundation of our background analysis is the assumption that the distribution of random halo field giants should be relatively smooth and slowly varying with distance. Indeed, if the Galactic halo follows anything close to an R^{-3} power law, as is widely assumed (and reported from the most recent surveys of blue horizontal branch stars; see a recent summary in Sluis & Arnold 1998), the counts of halo giants per unit solid angle should be flat, modulo second order effects relating to possible metallicity gradients (which are generally not found in the outer halo; Searle & Zinn 1978, Zinn 1985, Carney et al. 1990, Armandroff, Da Costa & Zinn 1992, Rich 1998). In our case, we count giant stars *already pre-selected (on the basis of their position in the color-color diagram) to be metal-poor*; if we adopt a counting filter in the CMD with a shape matching the CMD selection box in Figure 6 (which follows the outline of an [Fe/H]~ -2 RGB) our magnitude counts of these giants translate more or less directly into counts by distance modulus.

Thus, we offset the CMD bounding box of Figure 6 by 0.5 magnitude intervals, and at each offset position count the number of giants satisfying the color-color criterion shown in Figure 4. These counts are summarized for each of our four magnitude-limited data sets in Figure 12 (which shows all metal-poor, color-color selected giants) and Figure 13 (which shows only those metal-poor, color-color selected giants outside the IH95 tidal radius). Note that the actual filter used for each panel in Figures 12 and 13 was modified to take into account the varying depths of the four magnitude-limited data sets. For example, in the $M < 19.3$ data set, the bottom of the CMD bounding box is truncated precisely at $M = 19.3$. In turn, the $M < 19.8$ data set is analyzed with the appropriately truncated CMD bounding box at $M = 19.8$, and etc. For each magnitude-limited data set, the modified, truncated bounding box is the one offset and used to produce the giant count histograms in Figures 12 and 13. Note that only offsets in the direction of brighter magnitudes make sense, as offsets in the fainter direction incorrectly evaluate the numbers of stars due to sample incompleteness at the faint end. The maximum negative magnitude offset was given by the bright-end, CCD-saturation limit of the survey.

The main feature to note in each panel of Figure 12 and 13 is the relatively flat contributions of stars at magnitudes brighter than the Carina RGB. Indeed, under the assumption that the majority of these stars are giant stars and not dwarfs with large photometric errors or low [Fe/H], *the high degree of flatness in the histograms strongly supports an R^{-3} distribution for Galactic halo field giants (or at least metal-poor giants).* We assume this flatness persists through the magnitude range dominated by the Carina RGB ($\Delta M = 0$) in our survey, and adopt the mean level of the flat distribution as our background level of field halo giants and other interlopers in our "Carina-associated" giant sample at $\Delta M = 0$.

As the magnitude offsets approach 0 in each case shown in Figures 12 and 13, we see a sudden rise in the numbers of giants counted in the shifting counting box. The peak histogram values centered on $\Delta M = 0$ give the total number of stars in the Carina CMD bounding box as originally centered on the Carina RGB. But the sharpness of the rise seems to vary among the different samples. This is because there is some overlap of the shifted box with the true Carina RGB for small magnitude offsets and the maximum vertical extent of the bounding box varies: $\Delta M = 1.3$, 1.7, 2.1 and 2.5 magnitudes for the $M < 19.3$, $M < 19.8$, $M < 20.3$ and $M < 20.8$, respectively. If the "Carina-contaminated" bins less than these ΔM are ignored, we may determine the mean expected background contribution to our candidate Carina-associated stars from the various test offsets of the CMD bounding box in Figures 12 and 13. These data are included in Table 1.

Figure 12 shows that when all color-color selected metal-poor giants are considered regardless of their sky position in our survey, the number of expected contaminants lying within the Carina RGB is rather small: $< 4\%$ for all four magnitude limits explored. This suggests that, unless some peculiar problem is affecting our candidates specifically at the color-magnitude location of the Carina RGB, we might expect relatively high Carina membership probabilities from a spectroscopic follow-up study of these candidates (an expectation that is supported by our successful dwarf/giant discrimination of the Mateo et al. 1993, stars discussed at the end of §3.1 and shown in Figure 5, and by our spectroscopy in §3.5 below). Moreover, from the data in Figure 13 and Table 1 we see that the excess of candidate extratidal Carina-associated giants is at the level of 3.7σ or more for each of the four magnitude-limited data sets we explore.

A final observation to be noted from Figure 10 is that the extratidal distribution of Carina-like giant candidates appears rather isotropic, however, our field coverage is not ideal for assessing this. In contrast, Kuhn et al. (1996) report no extratidal Carina extension perpendicular to its major axis, but note that they explore only two minor axis fields 2° away from the Carina center. We also note some interesting similarities in the angular distribution of our Carina-associated giant candidates, particularly those in the $M < 19.8$ and $M < 20.3$ data sets (Figures 10b and 10c), and the isopleths published by IH95. In particular, the various spurs of higher density extending off of the IH95 central Carina contours and extending past the tidal radius (especially the spur to the southwest, but also the several other spurs at other position angles) are rather similar to such features in our data. Perhaps this is not surprising, as IH95's starcount analysis was essentially limited to counting Carina RGB members, albeit about a magnitude deeper than we have here. Nevertheless, the apparent general agreement in the two rather different analyses is encouraging.

3.5. Spectroscopy

Table 1 and Figures 10 and 13 suggest that we have found a significant "extratidal" population around Carina. A radial velocity survey to confirm whether these stars are indeed Carina-associated and, if so, to understand their velocity characteristics, is an obvious next observational step. While we have been unable to do such a study, we have managed to secure spectra of two of our Carina

giant candidates – both exterior to the IH95 tidal radius – during twilight time on nights allocated for other programs on the C100. With the remaining available telescope time, we also decided to observe two of the brighter, $(M - T_2)_o > 1.85$ stars that lie outside of the Carina CMD bounding box, but that do appear to be at the very tip of the Carina RGB (see discussion in §3.3). These stars yielded much better S/N spectra in the observing time available than the other two stars almost a magnitude fainter. One of these brighter stars is inside the tidal radius, while the other lies exterior. All four spectra were taken on the nights of UT 27 Aug to 1 Sep 1999 with the Modular Spectrograph. The wavelength range spans from approximately Hβ to Hα at ~ 1 Å pixel^{-1}. The spectrographic set-up and the radial velocity reduction procedures have been described elsewhere (Majewski et al. 1999d). We present the results of this analysis, and other data about the stars including the positions, the angular separation from the center of Carina, the magnitude and color, our derived radial velocities and the height of the radial velocity cross-correlation peak (see Majewski et al. 1999d), in Table 2. We show the positions of the four stars observed spectroscopically as triangle symbols in Figure 10a.

From repeat measures of previously well-observed stars during this observing run, we have determined our external, random and systemic velocity errors on the Carina candidate spectra to be $10 - 15$ km s^{-1}; this is sufficient to check association with Carina, but not good enough to make conclusions regarding possible differential velocity structure. The heliocentric radial velocity of Carina is 224±3 km s^{-1} (Mateo 1998) with a spread in the velocities of individual carbon stars and giants of about ±15 km s^{-1} (Lynden-Bell, Cannon & Godwin 1983; Mateo et al. 1993). Star C1407251, a bright giant candidate located within 16 arcmin of the Carina core, has a velocity that agrees with the Carina velocity and is certainly a member. Star C2103156, the bright giant star candidate that lies outside the IH95 tidal radius, gives a spectrum that looks remarkably metal-poor and very similar to that of star C1407251; the radial velocity for star C2103156 lies within 2σ of Carina's systemic velocity and we consider this giant candidate a likely member of the Carina system. Our spectra of stars C2103156 and C2501583, the two extratidal stars that were observed and that lie inside the Carina CMD bounding box, are also rather devoid of significant absorption lines which again suggests an association with Carina. Unfortunately, however, the combination of no strong lines and a weak and noisy signal make it hard to get a good radial velocity for these stars: We obtain marginal cross-correlation peaks that we generally regard as unacceptably small (< 0.3) and indicative of a several times larger random velocity error. Nevertheless, the derived heliocentric velocities are very close to Carina's (with C2501927 almost an exact match) and give rather poor matches to the expected velocity of foreground dwarfs, ~ 20 km s^{-1} (Mateo et al. 1993). We conclude the that latter two stars are far more likely to be associated with Carina than to be foreground stars.

We regard this small, but important test of four of our identified Carina-associated RGB candidates as vindication of our approach, and as support for our claims that the distribution of candidate Carina-associated giants in Figures 9 and 10 is most likely to reflect a real extended structure of the Carina dwarf. We hope to make further observations of additional extratidal

candidate stars with a larger aperture telescope.

3.6. Radial Profiles

We present "Carina RGB" starcounts as a function of elliptical annuli, along with the sampled areas in each annulus, in Table 3. The shape of the elliptical annuli were adopted from the parameters given by IH95, namely an ellipticity of 0.33 at a position angle of 65°. We space the width of our annular counting bins at one-fifth the major axis tidal radius given by IH95, except we use two times finer resolution in our first four bins. The r_{inner} and r_{outer} listed in Table 3 correspond to the inner and outer radius of the annuli along the major axis.

We convert the annular counts to densities (taking into account the actual survey area covered within each annulus) subtract the mean density of the background counts (derived from data in Tables 1 and 3 and presented in Table 3), and present the resultant radial densities (per arcmin^2) in Figure 14. To improve our signal-to-noise we combine into two bins our outermost eight annuli in Figures 14 and 15. The difference in the relative numbers of stars at each radius for our different magnitude-limited samples merely reflects the increase in the relative density of stars as a function of survey depth. In general, the counts from the different magnitude-limited data sets track each other at all radii (but, of course, the four data sets are not completely independent), though the $M < 19.3$ and $M < 19.8$ show more Poissonian scatter at large radii. We also include in Figure 14 the Carina count data as presented by IH95 (their Table 3), which has a magnitude limit almost another magnitude deeper than our $M < 20.8$ sample and which shows a commensurately higher density scaling. Our counts roughly track the IH95 counts, as well as the similarly deep Kuhn et al. (1996) starcount data also presented in Figure 14. Note that the IH95 data looses signal-to-noise after about 40 arcmin, at which point the background correction becomes critical, and IH95 limited their presentation to this radius (so we do so here as well). Even before 40 arcmin, however, the IH95 data show the effects of decreased signal-to-noise. On the other hand, our $M < 20.8$ data have reasonable signal-to-noise to almost 80 arcmin, at which point we are limited only by the extent of our survey sky coverage. Thus, our technique could potentially probe the extended structure of Carina to even greater radii than we have done here.

In order to compare results more readily, we normalize the relative densities in our four data sets to the IH95 data (Figure 15a). We normalize near the radius corresponding to our third annulus where our data have the highest counts (signal-to-noise). For the Kuhn et al. (1996) data, we normalize to the IH95 counts at the Carina core. The various data sets show general agreement in the character of the radial profile, especially within 20 arcmin. Moreover, as found by IH95 and hinted at in the counts by Demers et al. (1983), our data show a break in the fall-off rate of the radial counts near 20 arcmin, and this slower rate of decline continues to the radial limit of our survey area. However, the level of the counts in the IH95 data tend to be several times higher than ours in the outer radii of overlap (from about 13 to 40 arcmin), though this is where the IH95 data show large uncertainties and are most affected by their adopted background levels. Within our own

survey there is a trend in that the data sets with brighter magnitude limits have faster fall-offs at large radii than do the deeper data sets. This is likely a result of the fact that our brighter data sets face the problem of quantization noise at smaller radii than do the fainter data sets. Thus, for purposes of analysis at the largest radii, we take the $M < 20.3$ and $M < 20.8$ data sets as most likely to represent the true density profile (Figure 15b), though even these have some quantization noise at the outermost extent of our survey area.

The King profile (King 1962, 1966) fit by IH95 to the central region of their Carina data is also shown in Figure 15a, and highlights the dramatic break in our radial density rate of decline after about 20 arcmin. Our beyond-the-break counts of giants also approximately match the Kuhn et al. (1996) starcount data (which monitor excess populations only beyond the Carina break radius), though the latter also show more apparent scatter at large radii. This general match to the Kuhn et al. data to the limit of our survey is in spite of the fact that the Kuhn et al. data correspond only to fields along the Carina major axis. One might interpret this to suggest that our adoption of uniformly shaped and oriented elliptical annuli has little effect on the derived radial profiles, but we note that in our deepest data sets the sampling of azimuthal angles around Carina narrows to a range dominated by the Carina major axis, similar to the sampling by Kuhn et al.

3.7. Mass Loss Rate

Models of the radial distribution of the stars around a tidally disrupting satellite, e.g., by Johnston et al. (1999b, 2000), show characteristics very similar to those shown in Figure 15 (compare to Figure 15 of Johnston et al. 1999b). The Johnston et al. model demonstrates that the break point results from the contribution and eventual dominance of unbound stars. Dashed lines are included in Figure 15 past the tidal radius to represent various $r^{-\gamma}$-laws discussed by Johnston et al. (1999b, 2000). We present in Figure 15b only our deeper samples, for clarity in the comparison. It can be seen that our deeper survey data have a radial fall-off somewhere between $\gamma = 1$ and 2 to the limit ($\gtrsim 80$ arcmin) of our areal coverage.

Given the match of our data as presented in Figure 15 to the model predictions of Johnston et al. (1999b), we proceed for now under the assumption that past the radial profile break we are seeing unbound, extratidal debris, and calculate the mass loss rate using the formalism outlined in Johnston et al. (1999b). Note that even with "perfect" observations of their simulations Johnston et al. (1999b, 2000) found that they could only recover the rate of destruction of their satellites to within a factor of two. Hence the dominant source of uncertainty in our own calculation will be from the inherent simplicity of the model rather than observational errors, and the number we derive should be taken as an order-of-magnitude estimate of the destruction rate rather than a definitive measurement.

Because the Johnston et al. (1999b) formalism assumes complete area sampling in the derivation of the relative numbers of stars within certain annuli, we scale our counts of stars at each of our

annuli by the ratio of the total elliptical area to the amount of that annulus we actually surveyed. Under the Johnston et al. nomenclature, we adopt r_{break} as occurring between our sixth and seventh annuli (23 arcmin), the radius to which the extratidal debris is well-defined as $R_{xt} = 64$ arcmin (between our thirteenth and fourteenth annuli), and take for Carina's orbital parameters $g(\theta) = 1$ and $T_{orb} = 2\pi R_{GC}/(200\text{km/s})$ with $R_{GC} = 101$ kpc; this yields a mass-loss rate of $(\frac{df}{dt})_1 = 0.27$ Gyr^{-1}. This rather high value is relatively insensitive to the actual outer radial limit we take for the extratidal population, R_{xt}. We note that Johnston et al. who used the surface brightness at the location of r_{break} in the IH95 data to estimate the mass-loss rate with an alternative computational method, obtained $(\frac{df}{dt})_2 < 0.33$ Gyr^{-1}, an upper limit in agreement with our value. Carina and Ursa Minor have the largest estimated upper limits for mass loss rates among the dwarf galaxies discussed by Johnston et al. (all Milky Way dSph's excluding Sagittarius). The implication of a mass-loss rate of this order of magnitude is that Carina will not likely survive another Hubble time. Extrapolating backwards in time, one comes to the conclusion that Carina has likely lost a significant amount of mass already, and might be expected to sport significant tidal tails (see §4.3).

4. Discussion

4.1. Summary of Results

Our goal was to find evidence for, and begin mapping, tidal debris in the Carina dwarf galaxy by way of a search for Carina-associated giant stars to well beyond the nominal Carina tidal radius. We have used two criteria to select stars that are candidate giant stars associated with the Carina dwarf spheroidal: (1) colors in the $(M - T_2,\ M - DDO51)$ plane, where we are able to isolate evolved stars with [Fe/H] of order that of Carina, and (2) positions in the CMD that are similar to those of Carina giant branch and red clump stars. We check the background level of halo field giants, metal-poor subdwarfs masquerading as giants, and other possible interlopers, and find that they make a minor contribution to our signal. The latter stars, which we expect mainly to be random halo field giants, show a flat magnitude count slope, which suggests that they follow an R^{-3} law, as is commonly adopted for the halo.

We derive the radial profile of candidate Carina-associated giants, and find a break in the counts at about 20 arcmin, near the tidal radius derived by IH95 (who have better sampling and signal-to-noise in the Carina core). A well-established, 3.7σ excess of Carina-associated giant candidates is found beyond this radius, and spectroscopy of several of these stars verifies that they represent a real extended structure of Carina. The beyond-the-break stars show an $r^{-\gamma}$ decline in their radial fall-off, with $1 < \gamma < 2$, that is of a form similar to the predictions for unbound stars in tidally disrupting systems (Johnston et al. 1999b). Our excess of giant stars outside the King model cut-off radius may well represent stars that have recently been stripped from Carina due to Galactic tidal forces. Or they may represent still bound, retrograde revolving counterparts to those stars that *were* tidally stripped due to the fact that they happened to be in prograde

orbits when they became extratidal (Innanen & Papp 1979). Alternatively, if, as discussed in §1, modest amounts of dark matter prohibits the production of tidal tails, our Carina radial profile to > 80 arcmin heralds the need for an explanation of multiple component structures in dwarf spheroidals like Carina. Each of these alternatives has a distinct, kinematical signature that would be recognizable with an appropriate radial velocity survey.

Note that our search technique identifies *actual* dwarf galaxy-associated giant candidates and thus we are able not only to find radially-averaged galaxy profiles, but to make two-dimensional maps of the local overdensity of extended debris. In the case of Carina, since we observe viable candidates to the edges of our survey area, several times beyond the King model cut-off radius, it is possible that we are only seeing the beginnings of a wider diaspora of Carina stars that, if tidal debris, will eventually sort by relative energies into classic tidal tails at larger distances from Carina. This hypothesis must be followed up both by casting a wider photometric net for extratidal Carina giants at greater angular separations from the Carina core, and by testing whether the dynamics of present and future samples of "extratidal Carina-associated giants" have the proper, rotation-like radial velocity signature predicted for tidal debris. Unfortunately, we have been able to do the proper spectroscopic confirmations for only three extratidal stars, and so it is beyond the capabilities of the present paper to settle the thorny and weighty issues concerning dark matter, tidal debris and the true location of dwarf spheroidal tidal radii outlined in the Introduction. Instead, we choose to end our discussion by raising additional intrigue as to how Carina's extended populations may affect study of two of its neighbors – the Magellanic Clouds and the Milky Way.

4.2. Possible Connection to Apparent Tidal Debris Near the Magellanic Clouds

In a separate contribution from our program to study substructure in the halo, we discuss a targeted search for tidal stellar debris from the Magellanic Clouds (Majewski et al. 1999a; see Majewski et al. 1999c). The latter work includes observations in a partially-filled ring of fields encircling both Clouds. We have found coherent radial velocity structures among the distant giants identified in almost every field we have surveyed, which strongly suggests that there is tidal debris widely dispersed across the stretch of sky we have sampled in that survey (i.e., an envelope from 250° to 320° in Galactic longitude and from $-18°$ to $-55°$ in Galactic latitude). However, the strongest signal we have encountered – both in the excess in the density of giants identified as well as in the tightness of the coherence of the radial velocities of these stars – is among a set of six fields spanning a 15° arc located $\sim 18°$ from the center, and to the northeast, of the LMC (we term these fields LMC-NE here). The LMC-NE fields are placed directly between the LMC and Carina, with the surveyed arc of fields slicing across the arc connecting the LMC and Carina, 8/10 of the way from the LMC to Carina. It is too soon to ascribe the coherently moving stars in the LMC-NE fields as Magellanic in origin; however, their spatial and velocity distribution are not inconsistent with model expectations (Majewski et al. 1999a) for Magellanic debris, with a possible additional contribution of a moving group of stars from the LMC polar ring described by Kunkel et al. (1997).

These findings may be relevant to our findings here since the LMC-NE fields showing the distant moving group stars get as close as 3° from the center of Carina.

Note also that Carina lies near the Magellanic plane, along with the Clouds, Ursa Minor, Draco and a number of globular clusters, and some or all of these objects have been proposed to represent chunks of debris from the break-up of a formerly larger progenitor Magellanic system (Lynden-Bell 1976, Kunkel 1979, Palma, Majewski & Johnston 1999). In this scenario, these dwarf galaxy/globular cluster chunks would likely be awash in a debris stream of stars also pulled out of the progenitor. Thus, if Carina itself has an origin *as* tidal debris, we might expect coherent groups of stars nearby, whether drawn from Carina directly, or not. An argument against a picture as just painted is that tidal dwarf galaxies are not expected to contain dark matter (Barnes & Hernquist 1992, Moore 1996, Burkert 1997, Klessen & Kroupa 1998), whereas large dark matter contents ratios have been used to explain the high velocity dispersion of Carina stars (e.g., Mateo et al. 1993).

Whether Magellanic in origin or not, there *is* a blanket of coherently moving stars in the outer halo in this general direction of the sky and detected within 3° of Carina. It is worth checking whether this blanket extends to the position of Carina and contributes to the extratidal giant candidates we have found around Carina. However, given that there is a radial fall-off of stars with distance from *Carina*, we might not expect *all* of the extratidal Carina giants to be contributed by the LMC-NE feature. Clearly a more extensive survey of these stars from the LMC to Carina is needed.

4.3. Implications for the Structure and Origin of the Milky Way Halo

If Carina is losing stars, then the Milky Way halo is gaining them. Because of its age distribution, Carina presents an interesting case for the accretion of stars in the halo. If disintegrating, Carina should *presently* be contributing predominantly intermediate age ($\sim$ 7 Gyr) stars (Mould & Aaronson 1983, Mighell 1990) with a small admixture of stars from its old (12-15 Gyr) and young (2-3 Gyr) burst populations (Smecker-Hane et al. 1994, Grebel 1998, Mateo 1998). The derived proportional integrated star formation for these populations, based on Carina's present ratios of different aged stars, varies among authors but averages to ratios of old:intermediate:young approximately as 0.2:1.0:0.1. The youngest stars accreted from Carina may be comparable to the Preston et al. (1994) blue metal-poor stars, of which about half are thought to be relatively young stars from accretion events (Preston 1999, personal communication).

A comparison of the numbers of such young stars in Carina to the number in the Galactic halo has been used to provide an upper limit on the contribution of stars to the Milky Way by Carina or Carina-like, accreted galaxies: Unavane, Wyse & Gilmore (1996) calculate that at most approximately 60 dwarfs with the mass and metallicity of Carina could have been accreted by the Galactic halo, and would now account for a total of $\sim$ 3% of the mass of the halo. However, such

a calculation assuming a *static* Carina may greatly underestimate the potential contribution of matter to the Galactic halo via the accretion of dwarf galaxies.

The present mass loss rate we have determined (§3.7) suggests that Carina is now losing of order 27% of its mass every Gyr, and, since that rate was determined from the current distribution of luminous matter under a scenario where light traces mass, that fractional mass loss rate may be adopted for both the dark and luminous matter.[10] If we assume this fractional mass loss rate as typical over the life of Carina, then we approximate the mass of Carina N Gyr ago to be $(0.73)^{-N}$ larger than at present. Thus, we find that Carina was approximately a factor of 2, 10, and 100 times larger at the times of the bursts occurring approximately 2, 7, and 14 Gyr ago. Thus, Carina's predominant stellar contribution to the Milky Way may have been in the form of *old* stars from its first starburst.

This mass loss rate also suggests that, if having been maintained for the past Hubble time, accretion of Carina *alone* would have contributed about 6% of the Galactic halo's mass, and Carina itself would now be reduced to 1% of its original mass. Interestingly, Klessen & Kroupa (1998) find in N-body simulations of the tidal interaction of a satellite with a massive galaxy that the models converge to a dwarf remnant that has 1% of the mass of the initial satellite.

If Carina has been losing mass at this prodigious rate, then it has lost nearly all of the stellar component formed more than 7 Gyr ago. The loss of so much of the old stellar population could dramatically distort the observed star formation history (SFH) with respect to the actual SFH: The fact that 80% of the stars currently in Carina appear to be younger than the burst of star formation that occurred 7 Gyr ago (Hurley-Keller et al. 1998) could be ascribed to the fact that 90% of the mass of proto-Carina had already been accreted by the Milky Way by that time.

We thank Andi Burkert for helpful conversations. Chris Palma is gratefully acknowledged for his creation of the SKAWDPHOT program used for the photometric transformation solutions.

We are especially thankful for the support given this project by the Carnegie Observatories, both in Pasadena and at Las Campanas. The Director of the Carnegie Observatories, Dr. Augustus Oemler, has been especially kind with the granting of discretionary time, and with supporting SRM as a Visiting Associate of the Observatories. This telescope access has been particularly helpful as we have been unsuccessful obtaining telescope time for this project elsewhere.

JCO and SRM acknowledge several grants in aid of undergraduate research from the Dean of the College of Arts & Sciences at the University of Virginia. SRM acknowledges partial support from an National Science Foundation CAREER Award grant, AST-9702521, a fellowship from the David and Lucile Packard Foundation, and a Cottrell Scholarship from The Research Corporation.

[10]The luminosity of Carina is 4.3 x 10^5 $L_\odot$ and its total estimated mass is 1.3 x 10^7 $M_\odot$, which yields an integrated M/L of 31 (Mateo 1998).

REFERENCES

Aaronson, M. 1983, ApJ, 266, L11

Aaronson, M. & Olszewski, E. W. 1987, AJ, 94, 657

Armandroff, T. E., Da Costa, G. S. & Zinn, R. 1992, AJ, 104, 164

Barnes, J. A. & Hernquist, L. 1992, Nature, 360, 715

Beers, T. C. 1999, in The Third Stromlo Symposium: The Galactic Halo, eds. B.K. Gibson, T.S. Axelrod & M.E. Putman, ASP Conf. Ser. Vol. 165, (San Francisco: ASP), p. 202

Burkert, A. 1997, ApJ, 474, L99

Burkert, A. & Ruiz-Lapuente, P. 1997, ApJ, 480, 297

Cannon, R. G., Hawarden, T. G., & Tritton, S. B. 1977, MNRAS, 180, 81

Carney, B. W., Aguilar, L., Latham, D. W. & Laird, J. B. 1990, AJ, 99, 201

Da Costa, G. S. 1994, in ESO/OHP Workshop on Dwarf Galaxies, ed. G. Meylan & P. Prugniel (Garching: ESO), 221

Dekel, A. & Silk, J. 1986, ApJ, 303, 39

Demers, S., Beland, S., & Kunkel, W. E. 1983, PASP, 95, 354

Eskridge, P. B. 1988a, AJ, 95, 1706

Eskridge, P. B. 1988b, AJ, 96, 1352

Geisler, D. 1984, PASP, 96, 723

Geisler, D. 1990, PASP, 102, 344

Grebel, E. K. 1997, RvMA, 10, 29

Grebel, E. K. 1998, in IAU Symposium 192: The Stellar Content of Local Group Galaxies, eds. P. Whitelock & R. Cannon, ASP Conf. Ser. Vol. XX, (San Francisco: ASP), p. 1.

Grillmair, C. J. 1998, In *Galactic Halos*, ed. D. Zaritsky, ASP Conf. Ser. Vol. 136, (San Franciso: ASP), p. 45

Grillmair, C. J., Freeman, K. C., Irwin, M. & Quinn, P. J. 1995, AJ, 109, 2553

Hamlin, M. 1997, in Proper Motions and Galactic Astronomy, ed. R. M. Humphreys, ASP Conf. Ser. Vol. 127, (San Francisco: ASP), p. 137

Hargreaves, J. C., Gilmore, G. & Annan, J. D. 1996, MNRAS, 279, 108

Hargreaves, J. C., Gilmore, G., Irwin, M. J. & Carter, D. 1994, MNRAS, 269, 957

Harris, W. E., Fitzgerald, M. P. & Reed, B. C. 1981, PASP, 93, 507

Hodge, P. W. & Michie, R. W. 1969, AJ, 74, 587

Hurley-Keller, D., Mateo, M. & Nemec, J. 1998, AJ, 115, 1840

Innanen, K. A. & Papp, K. A. 1979, AJ, 84, 601

Irwin, M. & Hatzidimitriou, D. 1995, MNRAS, 277, 1354

Johnston, K. V. 1998, ApJ, 495, 297

Johnston, K. V., Majewski, S. R., Siegel, M. H., Kunkel, W. E. & Reid, I.N. 1999a, AJ, *in press*

Johnston, K. V., Sigurdsson, S. & Hernquist, L. 1999b, MNRAS, 302, 771

Johnston, K. V., Zhao, H., Spergel, D. N. & Hernquist, L. 1999c, ApJ, 512, 109

Johnston, K. V., Choi, P. & Guhathakurta, P. 2000, *in preparation*

King, I. R. 1962, AJ, 67, 471

King, I. R. 1966, AJ, 71, 64

Klessen, R. S. & Kroupa, P. 1998, ApJ, 498, 143

Kleyna, J., Geller, M., Kenyon, S. & Kurtz, M. 1999, AJ, 117, 1275

Kuhn, J. R. & Miller, R. H. 1989, ApJ, 341, L41

Kuhn, J. R., Smith, H. A. & Hawley, S. L. 1996, ApJ, 469, L93

Kunkel, W. E. 1979, ApJ, 228, 718

Kunkel, W. E., Demers, S., Irwin, M. & Albert, L. 1997, ApJ, 488, L129

Lynden-Bell, D. 1976, MNRAS, 174, 695

Lynden-Bell, D. 1982, Observatory, 102, 202

Lynden-Bell, D. & Lynden-Bell, R. M. 1995, MNRAS, 275, 42

MacLow, M.-M. & Ferrara, A. 1999, ApJ, 513, 142

Majewski, S. R. 1994, ApJ, 431, L17

Majewski, S. R. 1999, in The Third Stromlo Symposium: The Galactic Halo, eds. B.K. Gibson, T.S. Axelrod & M.E. Putman, ASP Conf. Ser. Vol. 165, (San Francisco: ASP), p. 76

Majewski, S. R., Munn, J. A. & Hawley, S. L. 1994, ApJ, 427, L37

Majewski, S. R., Kunkel, W. E., Ostheimer, J. C., Johnston, K. V. & Patterson, R. J. 1999a, *in preparation*

Majewski, S. R., Ostheimer, J. C. & Kunkel, W. E. 1999b, AJ, *submitted,* Paper I

Majewski, S. R., Ostheimer, J. C., Kunkel, W. E., Johnston, K. V., Patterson, R. J. & Palma, C. 1999c, in IAU 190: New Views of the Magellanic Clouds, eds. Y.-H. Chu et al, ASP Conf. Ser. Vol., *in press*

Majewski, S. R., Siegel, M. H., Kunkel, W.E., Reid, I.N., Johnston, K. V., Thompson, I.B., Landolt, A.U. & Palma, C. 1999d, AJ, *in press*

Mateo, M. 1998, ARA&A, 36, 435

Mateo, M., Olszewski, E., Pryor, C., Welch, D. L. & Fischer, P. 1993, AJ, 105, 210

Mateo, M., Olszewski, E. W., Morrison, H. L. 1998, ApJ, 508, L55

Mateo, M., Olszewski, E., Vogt, S.S. & Keane, M.J. 1998, AJ, 116, 2315

McClure, R. D. 1976, AJ, 81, 182

Mighell, K. J. 1997, AJ, 114, 1458

Milgrom, M. 1983a, ApJ, 270, 365

Milgrom, M. 1983b, ApJ, 270, 384

Moore, B. 1996, ApJ, 461, L13

Mould, J. & Aaronson, M. 1983, ApJ, 273, 530

Norris, J. E. 1999, in The Third Stromlo Symposium: The Galactic Halo, eds. B.K. Gibson, T.S. Axelrod & M.E. Putman, ASP Conf. Ser. Vol. 165, (San Francisco: ASP), p. 213

Oh, K. S., Lin, D. N. C. & Aarseth, S. J. 1995, ApJ, 442, 142

Olszewski, E. W., Aaronson, M. & Hill, J. M. 1995, AJ, 110, 2120

Olszewski, E.W., Pryor, C. & Armandroff, T.E. 1996, AJ, 111, 750

Palma, C., Majewski, S. R. & Johnston, K. V. 1999, ApJ, *submitted*

Paltoglou, G. & Bell, R. A. 1994, MNRAS, 268, 793

Piatek, S. & Pryor, C. 1995, AJ, 109, 1071

Preston, G. W., Beers, T. C. & Schectman, S. A. 1994, AJ, 108, 538

Pryor, C. T. 1999, in Galaxy Dynamics, eds. D.R. Merritt, M. Valluri & J.A. Sellwood, ASP Conf. Ser. Vol., *in press*

Pryor, C. & Kormendy, J. 1990, AJ, 100, 127

Reid, N. & Majewski, S. R. 1993, ApJ, 409, 635

Rich, R. M. 1998, in Abundance Profiles: Diagnostic Tools for Galaxy History, eds. D. Friedli, M. Edmunds, C. Robert & L. Drissen, ASP Conf. Ser. Vol. 147 (San Francisco: ASP), p. 36

Schlegel, D. J., Finkbeiner, D. P. & Davis, M. 1998, ApJ, 500, 525

Searle, L. & Zinn, R. 1978, ApJ, 225, 357

Seitzer, P. & Frogel, J. A. 1985, AJ90, 1796

Sluis, A. P. N. & Arnold, R. A. 1998, MNRAS, 297, 732

Smecker-Hane, T.A., Stetson, P.B., Hesser, J.E. & Lehnert, M.D. 1994, AJ, 108, 507

Smecker-Hane, T.A., Stetson, P.B., Hesser, J.E. & Vandenberg, D.A. 1996, in From Stars to Galaxies: The Impact of Stellar Physics on Galaxy Evolution, ed. C. Leitherer, U. Fritz-von-Alvensleben & J. Huchra, ASP Conf. Ser. Vol. 98, (San Francisco: ASP), p. 328.

Smecker-Hane, T.A., Mandushev, G.I., Hesser, J.E., Stetson, P.B., Da Costa, G.S. & Hatzidimitriou, D. 1999, in Spectrophotometric Dating of Stars and Galaxies, eds. I. Hubeny, S. Heap & R. Cornett, ASP Conf. Ser., (San Francisco: ASP), *in press*

Stetson, P. B. 1992, in Astronomical Data Analysis Software and Systems, eds. D.M. Worrall, C. Biemesderfer & J. Barnes, ASP Conf. Ser. Vol. 25, (San Francisco: ASP), p. 297

Suntzeff, N.B., Mateo, M., Terndrup, D.M., Olszewski, E.W., Geisler, D. & Weller, W. 1993, ApJ, 418, 208

Toomre A. & Toomre J. 1972, ApJ, 178, 623

Unavane, M. Wyse, R. F. G. & Gilmore, G. 1996, MNRAS, 278, 727

van Agt, S. L. Th. 1978, Publ. D. Dunlop Obs., 3. 205

Vogt, S. S., Mateo, M., Olszewski, E. W. & Keane, M.J. 1995, AJ, 109, 151

Zinn, R. 1985, ApJ, 293, 424

This preprint was prepared with the AAS LaTeX macros v5.0.

Captions

Fig. 1.— Map of all detected objects in our survey region centered on Carina. Squared regions indicate boundaries of individual C40 frames, whereas round regions are those surveyed with the C100 WFC. The ellipse is the 29 arcmin tidal radius at position angle 65° derived by IH95. Solid lined boundaries indicate frames that are fully photometric and tied to standard stars. These were used to bootstrap the photometry for the other fields shown with dashed line boundaries.

Fig. 2.— Photometric errors for stellar objects in the survey fields as a function of magnitude for the (a) C40 and (b) C100 data.

Fig. 3.— Dereddened $(M - T_2, M)_o$ color magnitude diagrams for the (a) C40 data and (b) C100 data. In (c) and (d) only objects detected with stellar profiles and with magnitude errors less than 0.1 mag in all filters are included for the (c) C40 and (d) C100 data.

Fig. 4.— $(M - T_2, M - DDO51)_o$ diagrams for all of the (a) C40 and (b) C100 data in the present survey. Only objects detected with stellar profiles and with magnitude errors less than 0.1 mag in all filters are included. The *solid line* shows the bounding region we have employed to select metal poor giant star candidates. The curves (adapted from Paltoglou & Bell 1994) show the expected location of dwarfs and giants; for clarity we break up the curves by panel as (a) giants (with abundances, from top to bottom: [Fe/H]$= -3.0, -2.0, -1.0, 0.0$) and (b) dwarfs (with abundances from top to bottom: [Fe/H]$= -3.0, -2.0, -1.0, +0.5$) (see Paper I).

Fig. 5.— (a) $(M - T_2, M)_o$ diagram for the C40 CCD frame centered on Carina with the candidate Carina RGB stars from Mateo et al. (1993) marked. The stars that have radial velocities measured by Mateo et al. consistent with Carina membership are indicated by filled circles, while the stars with radial velocities consistent with their being foreground dwarfs are indicated by open circles. (b) $(M - T_2, M - DDO51)_o$ diagram for the same data. The spectroscopically confirmed Carina RGB stars lie comfortably within the giant box indicated in Figure 4, while the Mateo et al. foreground dwarfs land precisely on the expected locus for $-1.0 \leq$ [Fe/H] $< +0.5$ dwarfs (see Figure 4b).

Fig. 6.— $(M - T_2, M)_o$ color-magnitude diagram for stars selected as metal-poor giants in Figure 4 and within 10 arcminutes of the center of Carina. Panel (a) shows the C40 data and panel (b) shows the C100 data. The "box" shown by the solid lines is our CMD selection criterion for "Carina-associated RGB stars".

Fig. 7.— $(M - T_2, M - DDO51)$ diagram with stars selected by the bounding box for the Carina RGB in Figure 6 shown as X's. Panel (a) shows the C40 data and (b) shows the C100 data.

Fig. 8.— $(M - T_2, M)_o$ color-magnitude diagram for all stars selected by the two-color selection criterion shown in Figure 4. The CMD bounding box defined from Carina stars within its core radius is shown by the solid lines.

Fig. 9.— (a) Distribution on the sky of all stars selected as "Carina-like" giants by *both* the final color-color and color-magnitude selection criteria. (b) Distribution on the sky of all stars with positions in the color-color diagram within the bounding box in Figure 4, but *not* within the color-magnitude bounding box defined in Figure 6. As before, the *solid lines* indicate frames that were taken under photometric conditions and *dashed lines* indicate those that were not.

Fig. 10.— Sky distribution of all stars selected as "Carina-like" giants by *both* the final color-color and color-magnitude selection criteria for the magnitude limits (a) $M < 19.3$, (b) $M < 19.8$, (c) $M < 20.3$ and (d) $M < 20.8$. In each panel we show the boundaries of, and candidates from, only those CCD survey areas that are complete to the magnitude limit indicated. The four triangles in panel (a) mark the positions of the four spectroscopically observed stars listed in Table 2 and discussed in §3.5.

Fig. 11.— Same as Figure 10, but for those stars selected as "Carina-like" giants by color-color, but *not* color-magnitude criteria.

Fig. 12.— Counts of giant candidates selected as low-metallicity giants by the color-color selection criterion in Figure 4 as a function of the M band magnitude offset, ΔM, of the CMD bounding box in Figure 5.

Fig. 13.— Same as Figure 12, but for extratidal giant candidates only.

Fig. 14.— Radial profile of the density (per arcmin^2) of candidate Carina-associated giants for the $M < 19.3$ (*open triangles*), $M < 19.8$ (*solid triangles*), $M < 20.3$ (*open circles*) and $M < 20.8$ (*solid circles*) samples. For some points at small radii, the error bars are smaller than the plotted symbol. The *asterisks* are the background-subtracted counts as presented in IH95. The *stars* show the results from Kuhn et al. (1996). In the IH95 and our own data, we have combined some of the outer radial bins to increase signal-to-noise.

Fig. 15.— (a) Radial profile of the density of candidate Carina-associated giants combined with IH95 starcounts and all normalized at 8.7 arcminutes. Symbols are as in Figure 14. The solid line shows the King profile as obtained from the data in IH95. The dashed lines show $r^{-\gamma}$ fall-offs in the "extratidal domain", with γ =1,2 and 3 and with normalization to our seventh bin. We have combined some of the larger radius bins in our survey and in IH95 to increase signal-to-noise. (b) Same as (a), but for only our $M < 20.3$ and $M < 20.8$ samples.

Table 1. Total Carina-Associated Giant Candidates and Expected Background Counts

Magnitude limit	Total Counts	Background	Extratidal Counts	Extratidal Background
$M < 19.3$	223	7.8 ± 2.9	26	7.1 ± 2.8
$M < 19.8$	385	15.0 ± 4.2	53	12.7 ± 3.1
$M < 20.3$	552	22.0 ± 4.3	89	18.0 ± 3.9
$M < 20.8$	800	31.0 ± 4.9	117	26.2 ± 4.7

Table 2. Radial Velocities of Carina-associated Giant Candidates

Name	R.A. (2000.0)	Dec.	r ($'$)	M_o	$(M - T_2)_o$	$(M - DDO51)_o$	R.V. (km s^{-1})	X-corr peak
C2501583	6 38 22.6	-51 10 59	34	18.32	1.68	+0.02	287.4	0.24
C2501927	6 38 37.0	-51 16 23	34	18.50	1.58	+0.04	223.1	0.20
C2103156	6 45 31.0	-50 49 26	37	17.76	2.00	−0.03	250.7	0.61
C1407251	6 40 08.8	-50 57 11	16	17.62	1.95	−0.01	233.1	0.77

Table 3. Radial Counts of Carina-Associated Giant Candidates

r_{inner} (arcmin)	r_{outer} (arcmin)	$M < 19.3$ count	$M < 19.3$ arcmin^2	$M < 19.8$ count	$M < 19.8$ arcmin^2	$M < 20.3$ count	$M < 20.3$ arcmin^2	$M < 20.8$ count	$M < 20.8$ arcmin^2
0.000	2.898	10	18	16	18	32	18	54	18
2.898	5.796	37	53	68	53	97	53	159	53
5.796	8.694	58	88	84	88	124	88	190	88
8.694	11.592	41	124	68	124	91	124	145	124
11.592	17.388	35	354	60	354	82	333	107	234
17.388	23.184	9	468	15	468	15	261	13	90
23.184	28.980	8	639	22	639	23	423	16	180
28.980	34.776	8	693	15	693	17	531	17	297
34.776	40.572	6	801	10	738	18	558	20	378
40.572	46.368	2	855	7	621	13	522	20	423
46.368	52.164	2	819	2	621	4	504	6	396
52.164	57.960	3	891	4	720	14	585	26	477
57.960	63.756	1	720	1	612	5	549	6	477
63.756	69.552	1	450	3	441	6	288	6	288
69.552	75.348	3	324	9	324	9	252	11	252
75.348	81.144	0	315	2	315	3	180	3	180
81.144	86.940	0	126	0	126	0	117	1	117
86.940	92.736	0	81	0	81	0	81	1	81
92.736	98.532	0	18	0	18	0	18	0	18
98.532	104.328	0	0	0	0	0	0	0	0
total area (deg^2)		2.18		1.96		1.52		1.16	
background (deg^{-2})		3.58		7.65		14.47		26.72	

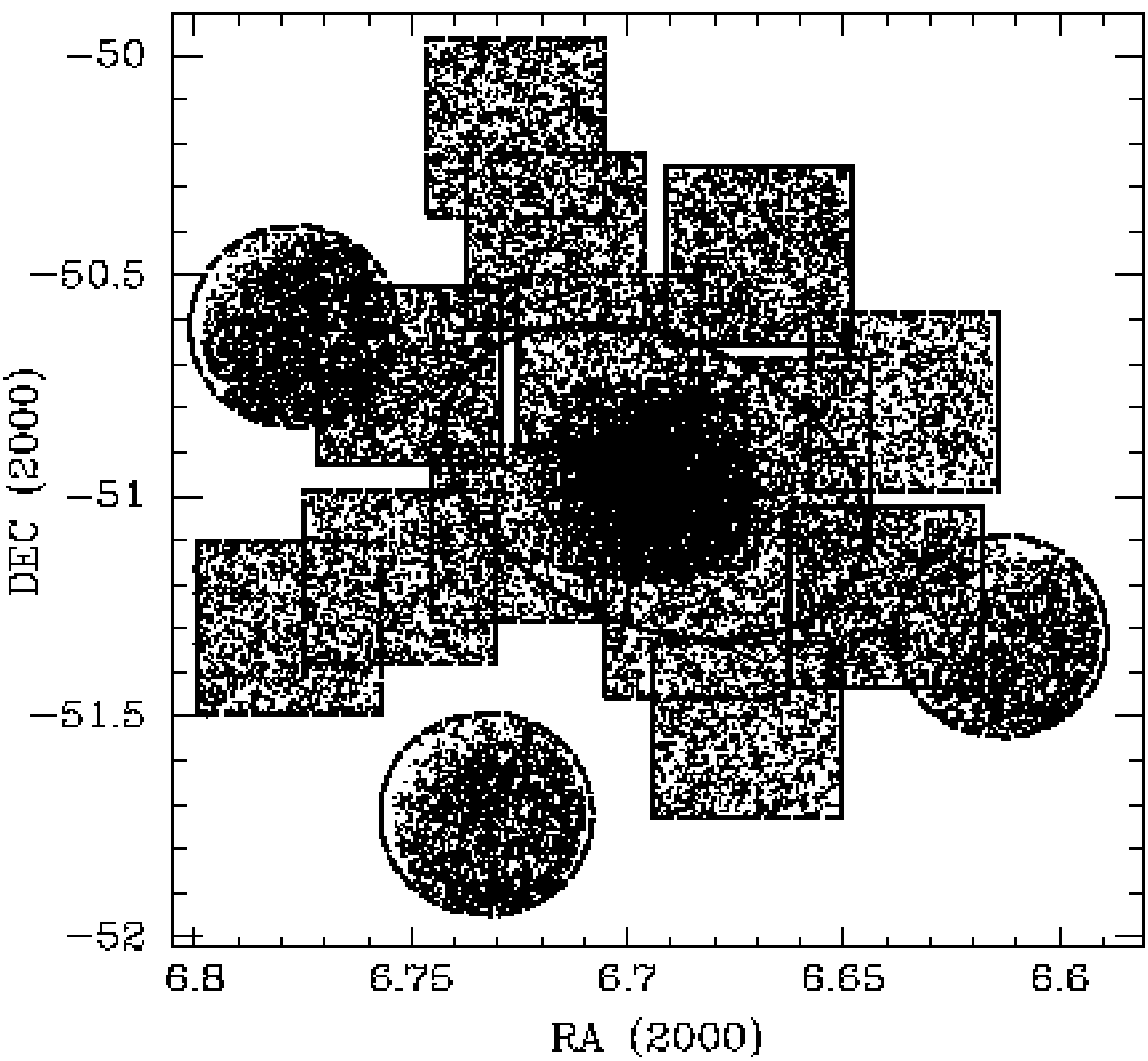

−50
−50.5
−51
−51.5
−52
DEC (2000)
6.8
6.75
6.7
6.65
6.6
RA (2000)

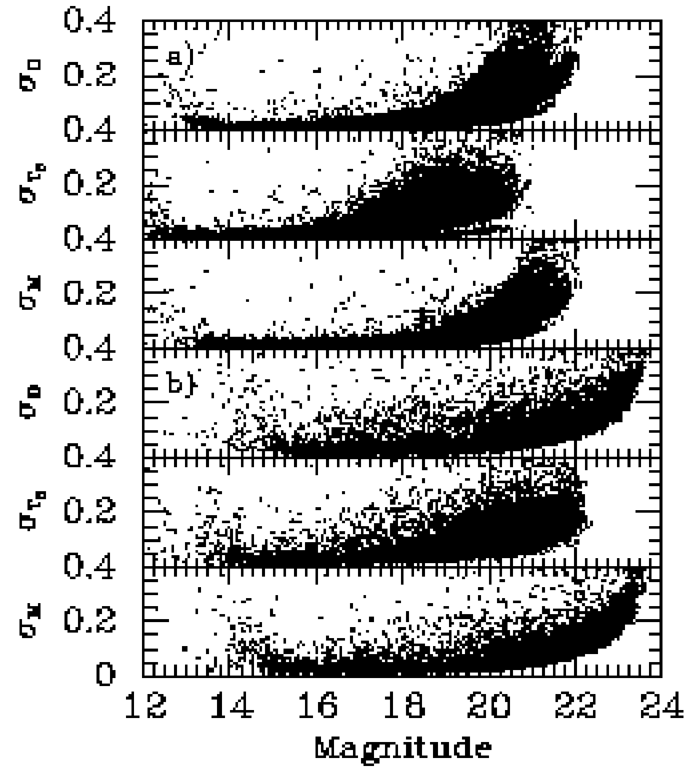
a)
b)
0.4
0.2
0
12
14
16
18
20
22
24
Magnitude

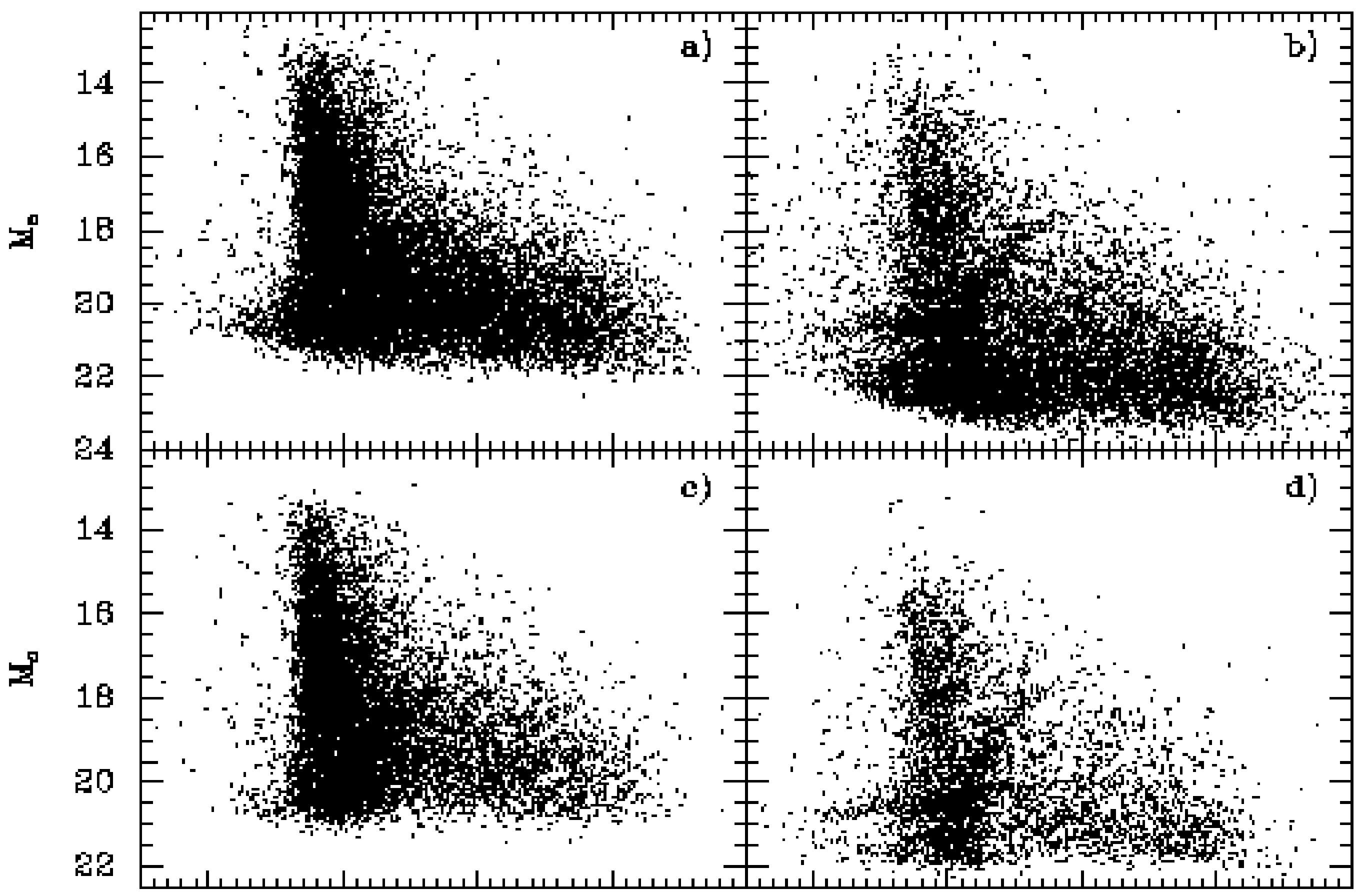

a)
b)
c)
d)
M_o
M_o
$(M-T)_o$
$(M-T)_o$

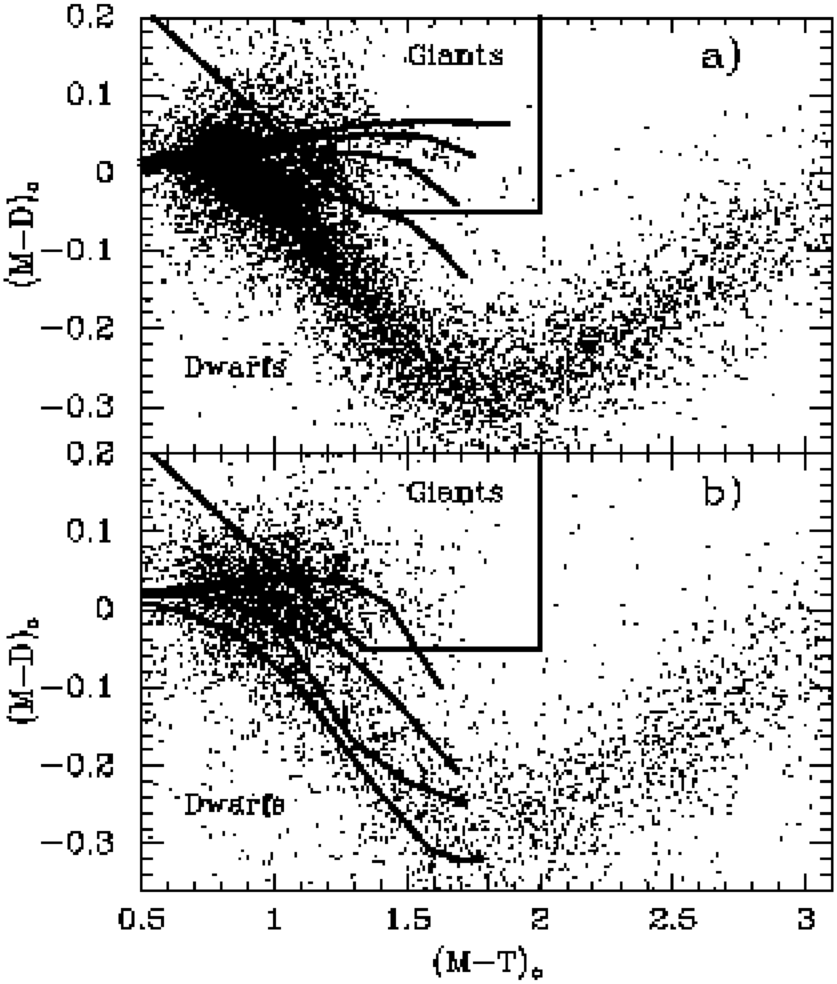

Giants
a)
Dwarfs
Giants
b)
Dwarfs
(M−D)o
(M−T)o
0.2
0.1
0
−0.1
−0.2
−0.3
0.5
1
1.5
2
2.5
3

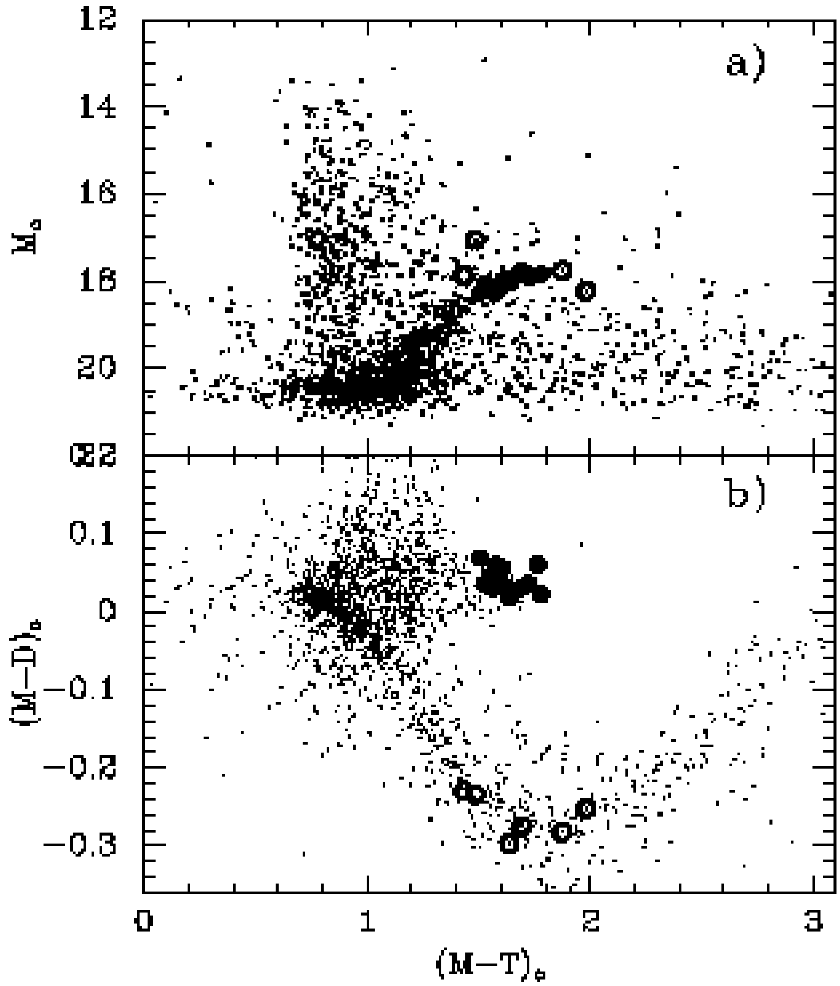

a)
b)
M_o
$(M-D)_o$
$(M-T)_o$

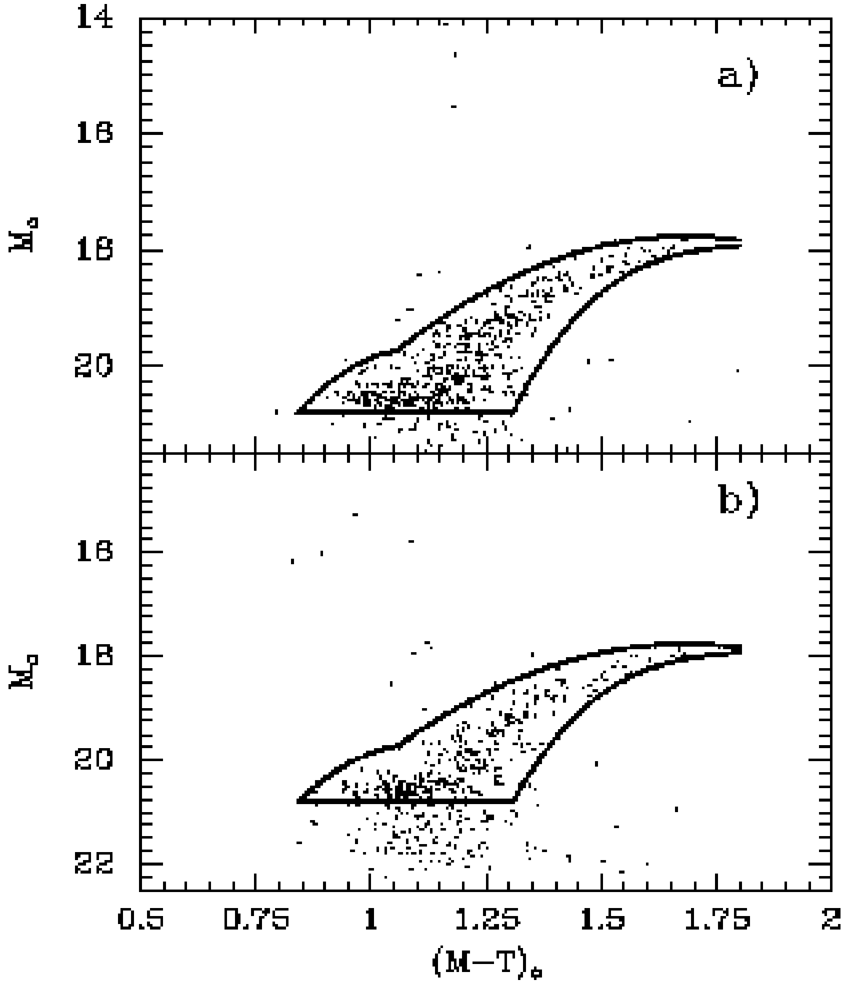
a)
b)
M_o
M_o
14
16
18
20
16
18
20
22
0.5
0.75
1
1.25
1.5
1.75
2
$(M-T)_o$

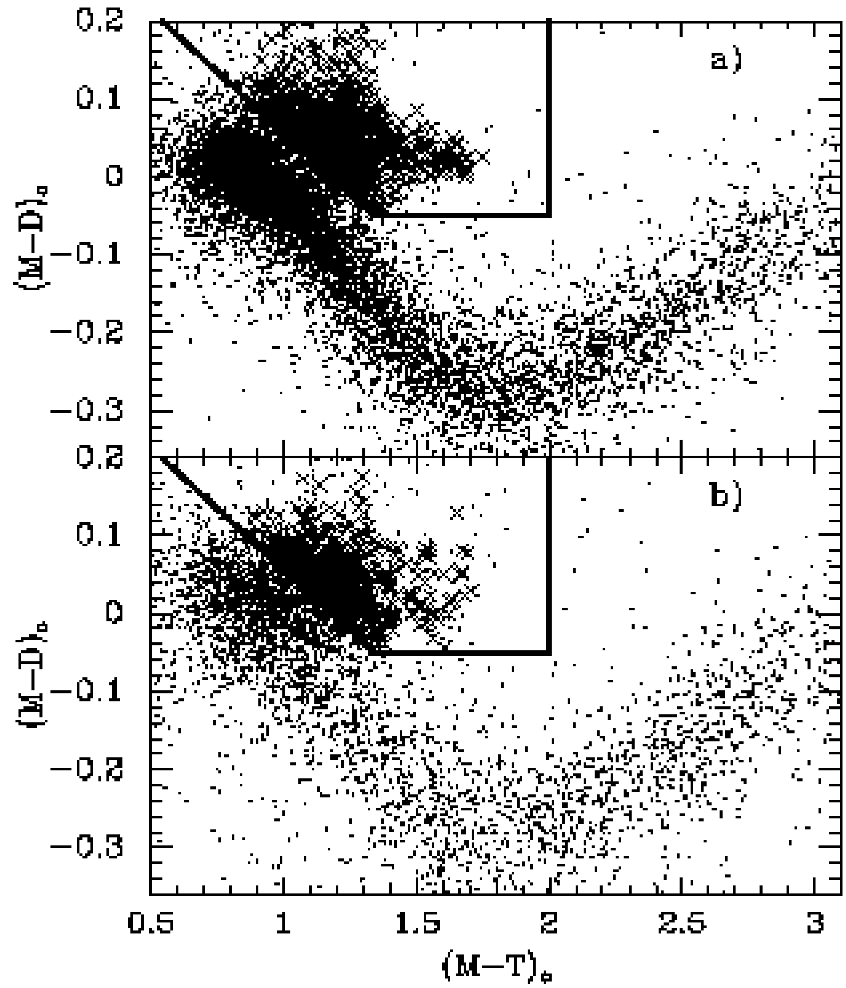

a)
b)
0.2
0.1
0
−0.1
−0.2
−0.3
$(M-D)_o$
0.5
1
1.5
2
2.5
3
$(M-T)_o$

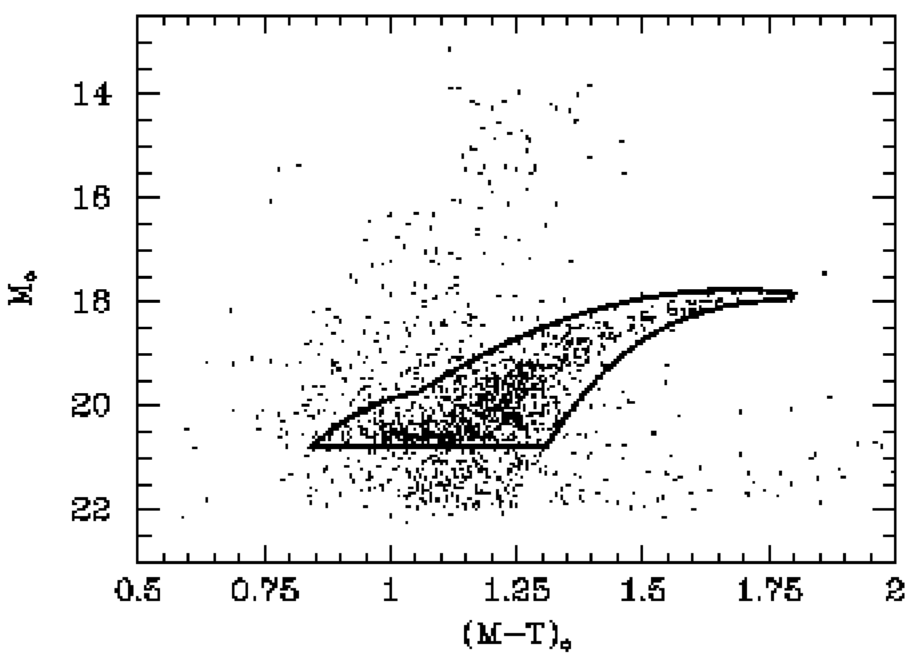

14
16
18
20
22
M_o
0.5
0.75
1
1.25
1.5
1.75
2
$(M-T)_o$

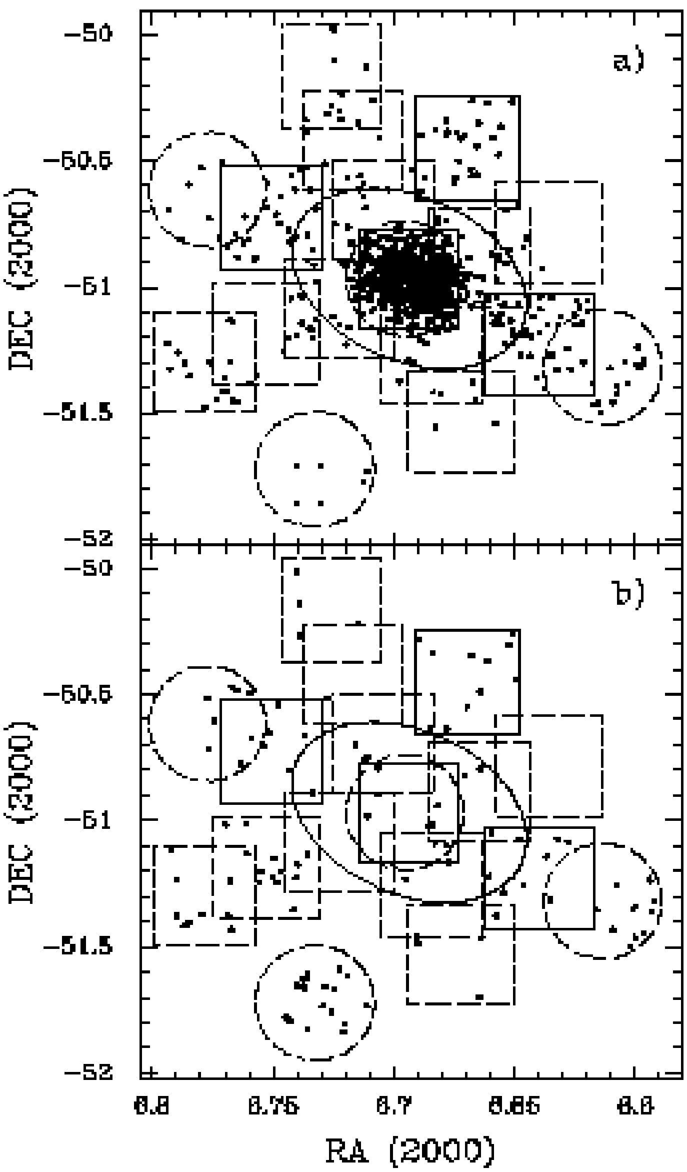

a)
b)
-50
-50.5
-51
-51.5
-52
DEC (2000)
6.8
6.75
6.7
6.65
6.6
RA (2000)

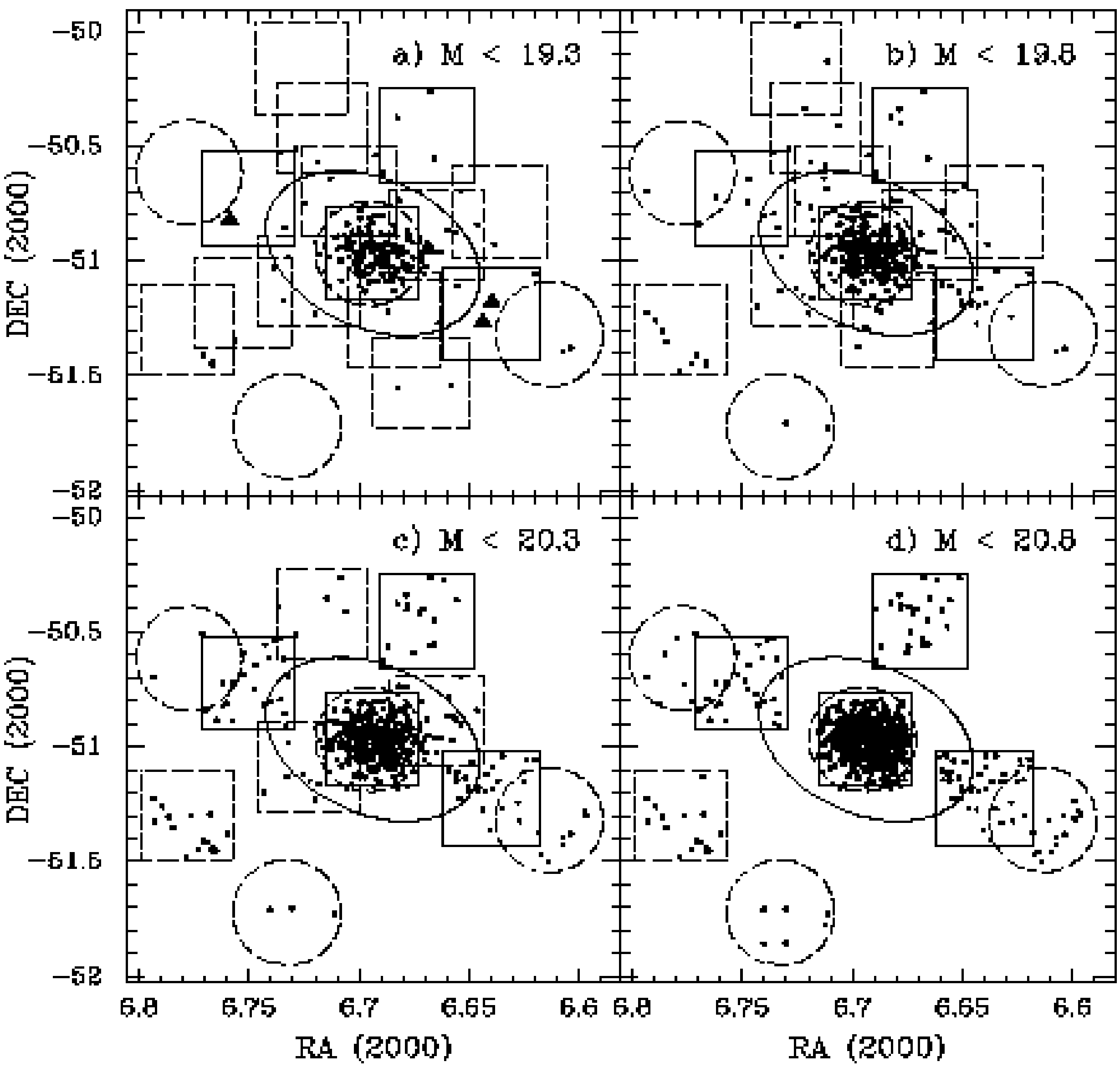
a) M < 19.3
b) M < 19.8
c) M < 20.3
d) M < 20.8
DEC (2000)
RA (2000)
−50
−50.5
−51
−51.5
−52
6.8
6.75
6.7
6.65
6.6

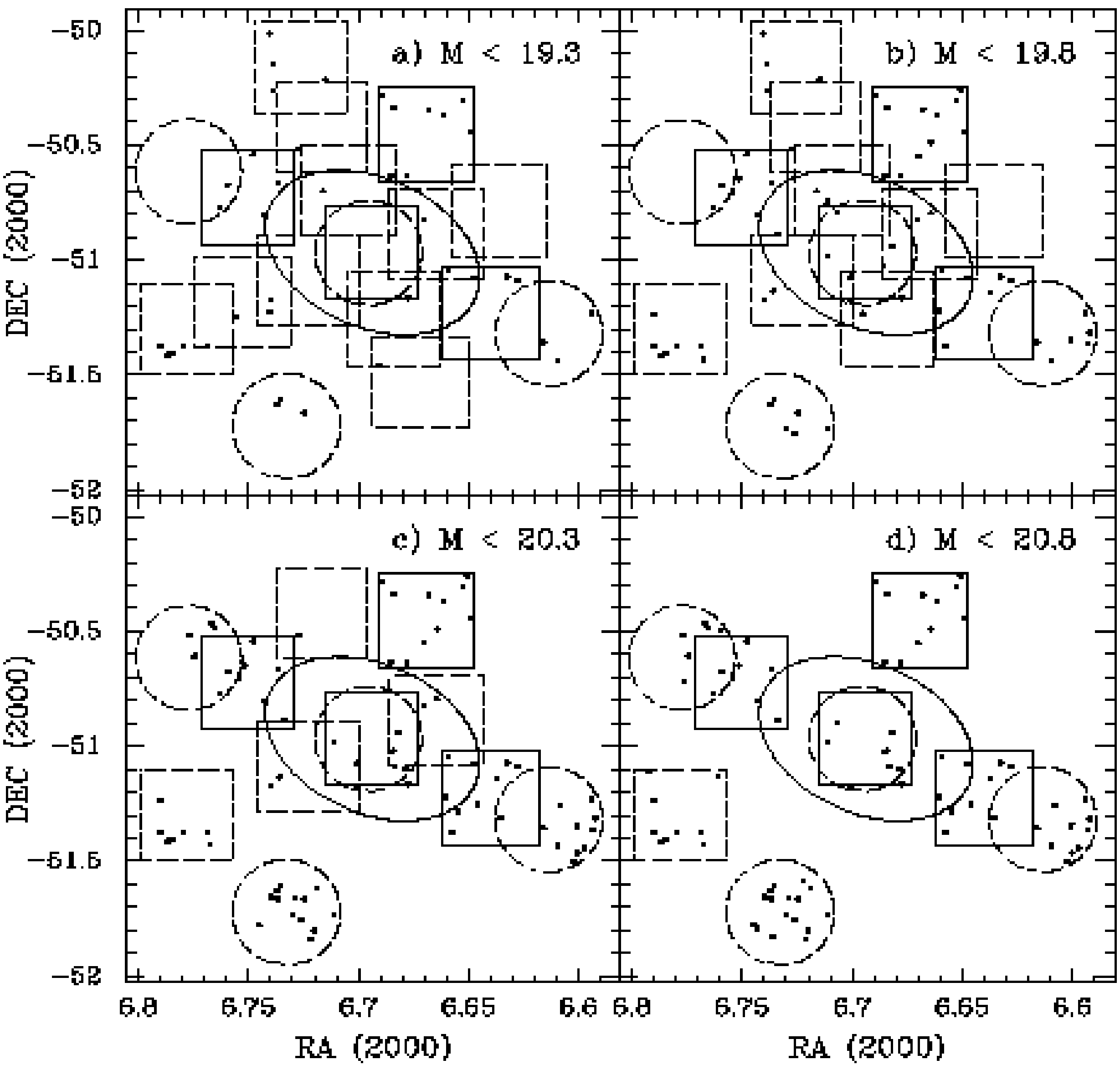
a) M < 19.3
b) M < 19.8
c) M < 20.3
d) M < 20.8
DEC (2000)
RA (2000)
-50
-50.5
-51
-51.5
-52
6.8
6.75
6.7
6.65
6.6

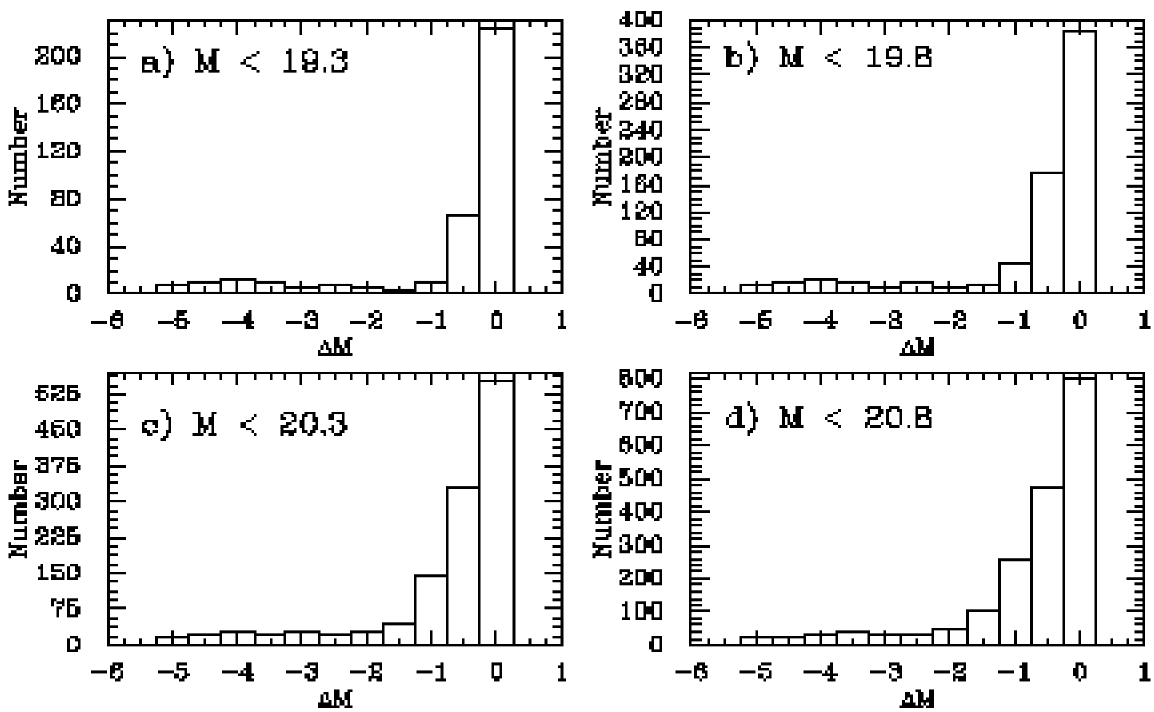
a) M < 19.3
b) M < 19.8
c) M < 20.3
d) M < 20.8
Number
ΔM

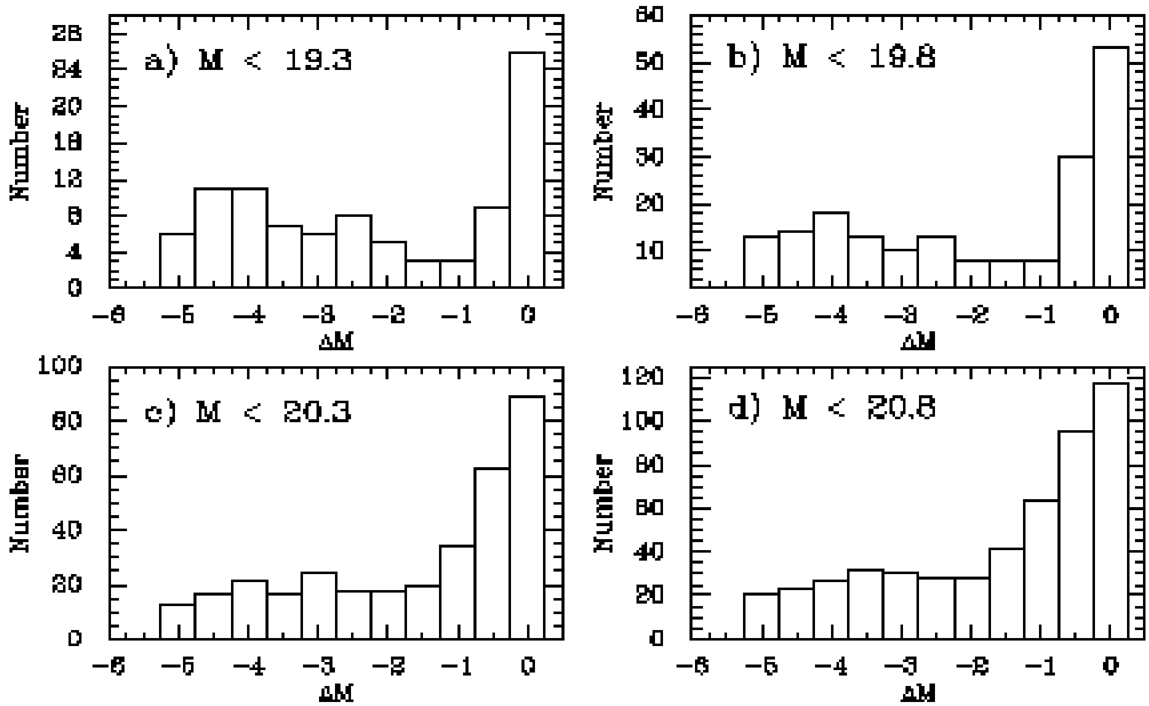

a) M < 19.3
b) M < 19.8
c) M < 20.3
d) M < 20.8
Number
ΔM

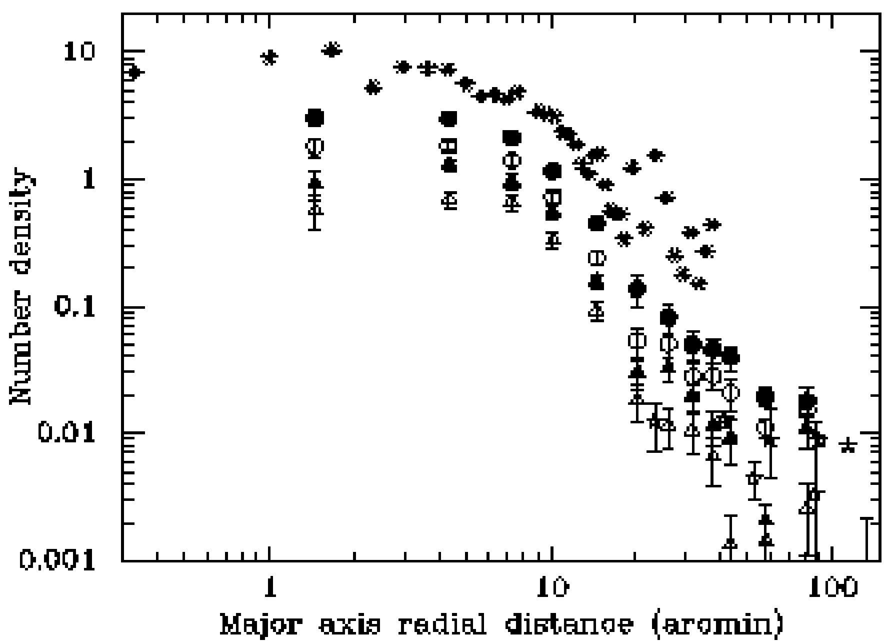
10
1
0.1
0.01
0.001
Number density
1
10
100
Major axis radial distance (arcmin)

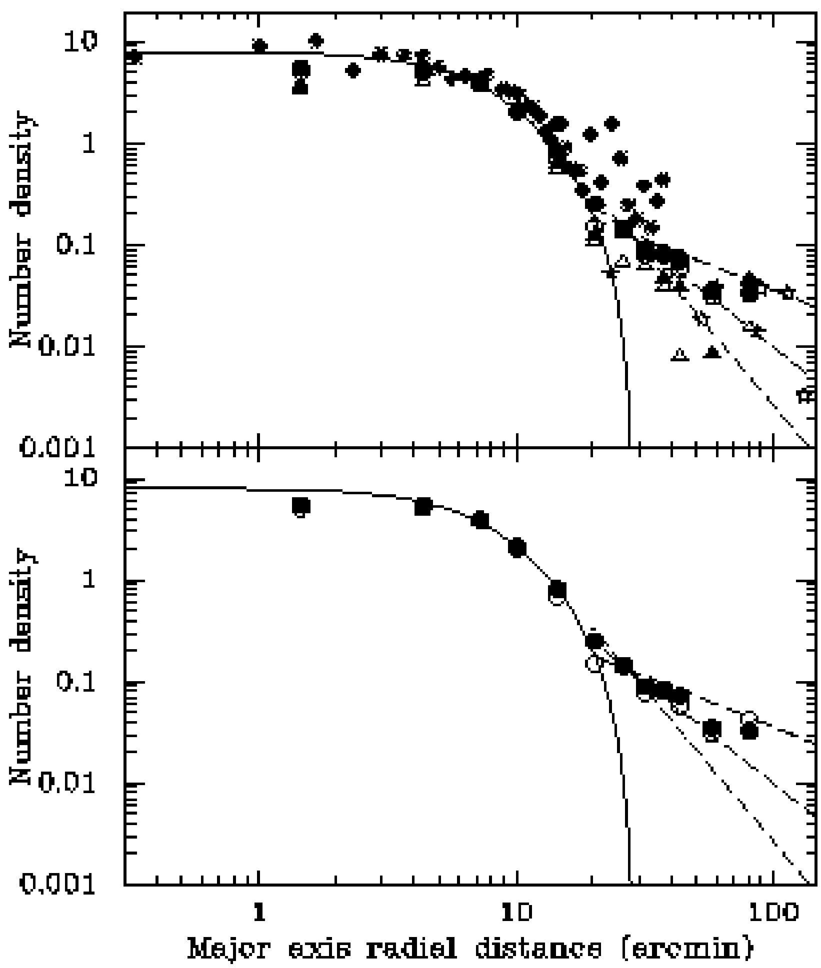
10
1
0.1
0.01
0.001
Number density
1
10
100
Major axis radial distance (arcmin)